Computationally modeling the impact of measured variance in skin mechanics on neural responses to touch stimuli

---

A Dissertation

Presented to

the faculty of the School of Engineering and Applied Science

University of Virginia

---

in partial fulfillment

of the requirements for the degree

Doctor of Philosophy

by

Yuxiang Wang

May

2016

APPROVAL SHEET

The dissertation

is submitted in partial fulfillment of the requirements

for the degree of

Doctor of Philosophy

_____
AUTHOR

The dissertation has been read and approved by the examining committee:

Gregory J. Gerling
_____
Advisor

Richard W. Kent
_____

Silvia S. Blemker
_____

Matthew B. Panzer
_____

Ellen A. Lumpkin
_____

_____

Accepted for the School of Engineering and Applied Science:

Craig H. Benson, Dean, School of Engineering and Applied Science

May
2016

Abstract

We rely on our sense of touch to obtain information from the external environment with which we interact. Upon touching an object, the distal mechanical stimulus propagates through the skin's layers toward the end organs of cutaneous afferents that initiate neural responses. While the encoding of various stimuli has been thoroughly investigated in prior studies, the impact of the skin's mechanics remains vastly understudied. In particular, while we know that the skin undergoes natural cycles of remodeling, we do not know how remodeling impacts the skin's thickness and elasticity and what impacts those might have on the neural response and neural sensitivity between afferents. In the first aim, we performed uniaxial compression tests to measure the viscoelastic properties of 139 mouse skin specimens while also varying stretch level and rate. This is the first effort to do such a detailed characterization at different stages of the hair cycle. Over the population measured, we observed the skin's thickness and viscoelasticity to be highly variable, yet found systematic correlations between the viscoelastic parameters and skin thickness and applied stretch. Specifically, residual stress ratio positively correlates with skin thickness and stretch, and relaxation time constants negative correlates with strain rates. In the second aim, we used the population of measurements to build finite element models to closely examine the effect of thickness-dependent viscoelasticity on the propagation of internal deformation toward the end orangs of slowly adapting type I (SAI) afferents. In simulating the observed changes to the skin's mechanics, we find that there can be large variance in stresses and strains near the locations of end organs, which might lead to large variance in firing sensitivity. However, variance in internal deformation is significantly reduced when the stimulus tip is controlled by surface pressure and compressive stress is measured near the end organs. The combined results of the two aims indicate that the skin can reliably convey surface stimulus information to locations of tactile receptors even amidst changes in skin's structure. During such

changes, stimulus control by surface pressure may be more naturalistic and optimal and underlie how animals actively explore the tactile environment.

Contents

1   Overview of aims

We rely on our sense of touch to obtain information about our environment. During cutaneous contact with an external object, the surface of our skin is deformed by distributed pressure or deflection. As surface forces propagate toward inward layers of skin, interior deformation fields of stresses and strains trigger neural responses from the end organs of mechanosensitive afferents. These responses are closely tied to the magnitude and decay of interior stresses and strains, dominated by the skin's mechanics. While we already know that the skin undergoes natural cycles of remodeling, one might assume that skin mechanics such as thickness and viscoelasticity will be impacted, and such impact influences the neural responses of tactile afferents. Herein, we seek to understand this question by combining uniaxial compression testing, finite element analysis and computational neuroscience models, decomposed into two aims of this dissertation. In the first aim, we quantified the skin viscoelasticity and how they vary, based on which the second aim investigated whether such variance will undermine the consistency of neural responses in tactile afferents.

Summary of the Aim I. We seek to quantify the variance in skin mechanics, specifically how their thickness and viscoelastic parameters distribute among a population of subjects in order to construct valid finite element model for predicting tactile afferent responses. We performed standard uniaxial compression test on a population of excised skin specimens from mouse hind limb. Ramp-and-hold displacement stimulus was applied on 139 skin specimens, harvested from 36 mice spanning different hair cycles to sample from a wide range of remodeling stages. A quasi-linear viscoelastic model with hyperelastic component was then fitted against stress-stretch-time recording in experiments to parameterize skin specimens. We analyzed distributions of skin

viscoelastic parameters, and find that they correlate with both skin thickness and experiment variables such as stretch level and rate. This quantification of skin compressive viscoelasticity over a population of skin samples is the first dataset available in the literature according to the best of the author's knowledge, and also served as the data input for the second aim.

Assumptions in Aim I. We assumed the skin to be isotropic, and only applied compressive loading that is perpendicular to the skin surface during experiments. Despite the fact that the skin is anisotropic [1], we used this assumption since we are collecting the data in the same direction with the dominant principal stresses in our numerical models to analyze the stress condition under indentations. In those cases, the maximum principal compressive stresses are perpendicular to the skin surface and dominates over other directions. In addition, we used hairy rather than glabrous skins, which are more complex and anisotropic due to the intermediate ridges [2]. Therefore, we may use this assumption to simplify our analysis without much loss in accuracy for our stress analysis.

Summary of the Aim II. Within a class of cutaneous afferents, one might assume the variability in firing between-units could be due to dramatic changes during renewal of the skin's thickness and elasticity. To understand this connection, we constructed a computational model for the SAI afferent under indentation, which consists a finite element sub-model and a neural dynamics sub-model. We considered the skin properties of six mice that span a representative cohort from the data collected in the first aim. In modeling the propagation of the surface stimulus to the interior of the skin, we find that there can be large variance in stresses and strains near the locations of end organs, which can lead to large variance in sensitivity. However, variance is significantly

reduced when the stimulus tip is controlled by surface pressure and compressive stress is measured near the end organs. Amidst changing skin mechanics, stimulus control by surface pressure and interior deformation of stress may be more naturalistic and optimal and underlie how we actively explore our environment. This is the first study that showed the skin can reliably convey surface stimulus even amidst changes in skin mechanics, and mechanistically explained that the surface pressure and interior stress are the most naturalistic for SAI afferents.

Assumptions in Aim II. In this analysis, we have made two major assumptions. Firstly, we assumed that the skin viscoelasticity can be adequately characterized by the quasi-linear viscoelastic model. This differs from our finding in Aim I where skin exhibits viscoelasticity dependent on the stretch level and rate; however, this mainly impacts the within-skin comparison across stimulus levels, whereas in this analysis all comparisons were done between skin specimens under the same stimulus. Secondly, we assumed constant neural dynamics between fibers, which is obviously not true. Nevertheless, this avails us to fully utilize the power of simulation and control the intrinsic uncertainty in the neurons, which facilitates us to focus our analysis on only the impact from skin mechanics.
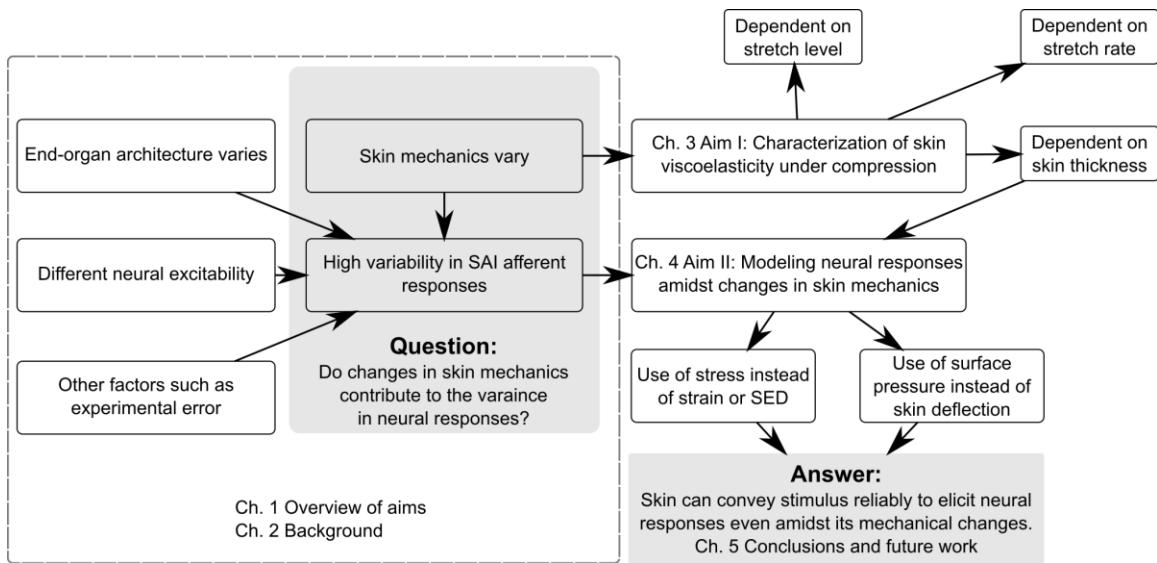
Figure 1.1 Flowchart of the dissertation.

Organization of this dissertation. The flowchart above (Figure 1.1) illustrates the organization of this dissertation. In Ch. 1&2, we propose our research question in the context of our knowledge base: do changes in skin mechanics contribute to the variance in neural responses? This question was addressed in two aims: Ch. 3 quantifies the changes in skin mechanics with uniaxial compression testing, and Ch. 4 uses computational modeling to investigate how such changes impact neural responses. Finally, in Ch. 4.5 we conclude that the skin can convey surface stimulus reliably to elicit neural responses, even amidst skin mechanical changes.

2   Background

We learn about object features that we contact via arrays of tactile afferents. When an object forms a surface stimulus on the skin (Figure 2.1A), it propagates the distributed pressure or deflection into a stress-strain fields inside (Figure 2.1B), and elicit trains of action potentials

(Figure 2.1C) from the mechanosensitive end-organs (Figure 2.1D) to pass localized stimulus information such as stimulus magnitude, rate and geometry to the central nervous system. In total, there are four types of mechanosensitive afferents in mammals: slowly adapting type I, slowly adapting type II, rapidly adapting, and Pacinian afferents, that each end in Merkel cells, Ruffini corpuscles, Meissner corpuscles and PC corpuscles [3], as illustrated in Figure 2.2. They each have their own structures and roles. For example, Pacinian corpuscles are large and composed of a series of tissue layers, which facilitate them to generate spikes to specifically encode high frequency vibration [4]. Meissner corpuscles, on the other hand, are much smaller and encode low frequency vibration to facilitate events such as slip for dexterous manipulation. In this study, we focus on the SAI afferents that are responsible for sustained stimulus to facilitate detection of edges and curvature. Its end-organs, Merkel cell-neurite complexes, are located at the intermediate ridges for glabrous skin and the touch dome in hairy skin [5], both between the epidermis and dermis on the epidermal side. In contrast to the SAII type of afferents, responses from SAI are highly irregular with a high coefficient of variation [6]. It responds to both moving and sustained stimulus, and have a much higher firing rate during the dynamic-ramp phase of a ramp-and-hold displacement stimulus compared to the sustained-hold phase [7]. Within a certain range, the firing rate of SAI afferents monotonically increases with larger applied displacements [8]; beyond this range when the stimulus continues to increase, the firing rates show suppression and monotonically decreases.
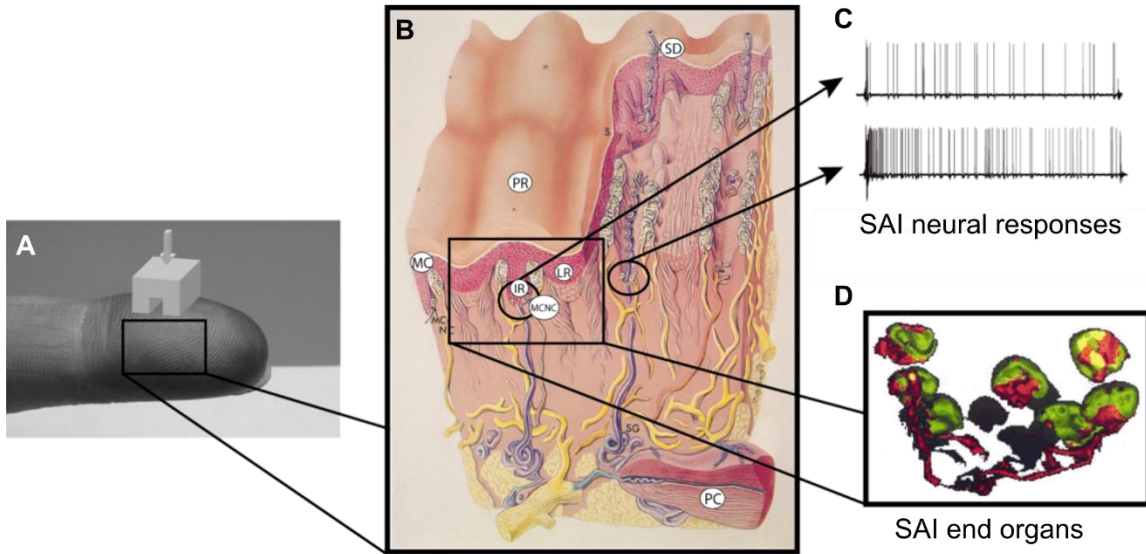
Figure 2.1 Propagation from surface stimulus (A) to interior deformation in the skin (B) that elicit neural responses (C) from the end organs of SAI afferents (D). Adopted from unpublished work by Dr. Gregory Gerling.
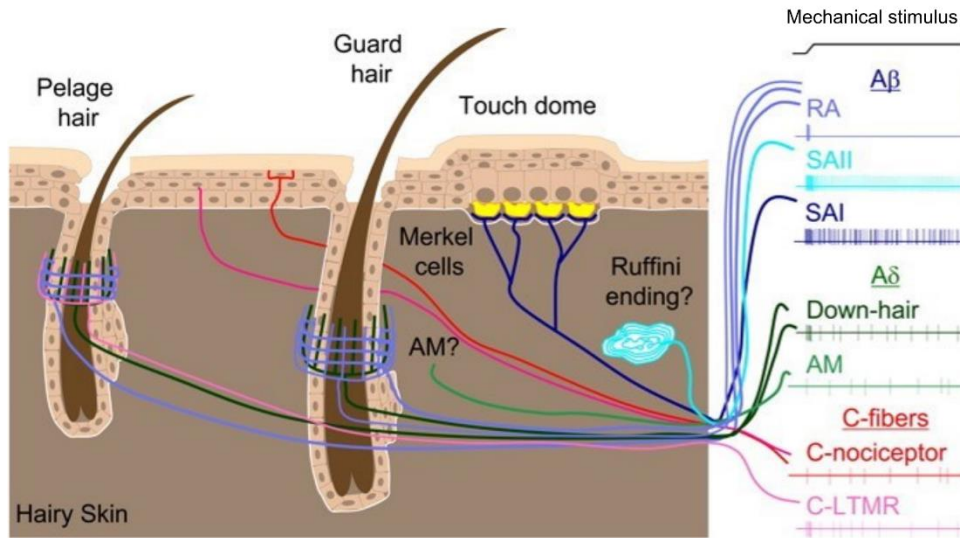
Figure 2.2 Tactile receptors in the hairy skin that innervates the mechanosensitive afferents. They respond to mechanical stimulus on skin surface with trains of action potentials, which we base our sense of touch [5].

It is natural for one to connect the skin mechanics to the neural response of SAI and other afferents. For this reason, past studies on mechanotransduction have carefully constrained skin materials used for the validity of the numerical models. The most commonly used method is to fit experimentally measured skin deflection under indentation to model predictions by adjusting skin mechanics parameters. Single-layered linear elastic model were first built analytically [9], followed by multiple-layer models where Young's modulus of epidermal, dermal and hypodermal tissues were each adjusted to fit skin deflection data [10,11]. For example, a 3-D primate fingertip model was constructed from measured external geometry, offset to obtain internal skin and bone layers, and eventually fitted to surface deflections under line loadings (Figure 2.3). While these work successfully depicted how mechanical cues flow through the skin and eventually generated responses from tactile afferents, it is unclear how sensitive these responses are when the skin mechanics changes. This is in part due to the difficulty in obtaining an accurate distribution of how skin mechanics vary through the computationally expensive model fitting method.
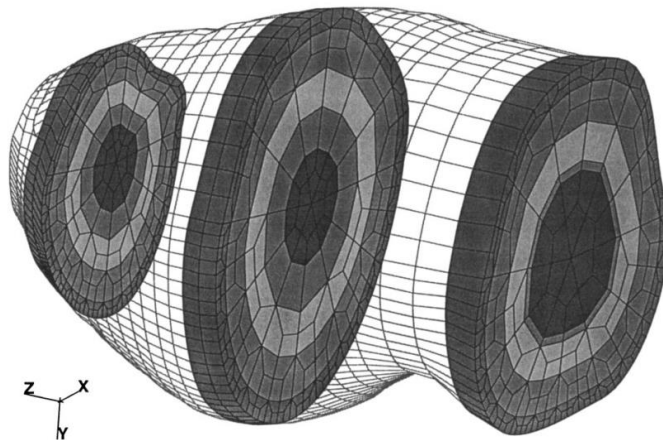
Figure 2.3 The monkey fingertip model with measured external geometry and offset counters for five layers. Three slices are shown, adopted from [11].

Nevertheless, skin mechanics are known to vary during an animal's life cycle. Past studies on human reported decreasing thickness and viscoelasticity with age [12–14]. On mouse skin, we also found that the skin thickness and stiffness is dependent on body weight, hair cycles and the skin site [15]. Unfortunately, these studies employed mostly indirect measures that are not constitutive parameters, and therefore cannot be directly plugged into finite element models. To investigate how these changes will impact tactile mechanotransduction, materials testing to generate standard constitutive parameters are needed. With a thorough search in the literature, the author noticed that although the skin's hyper-viscoelastic properties were thoroughly studied in tension [1,16–19], much less was done in compression, where they are likely to differ significantly between loading conditions. In addition, despite prior efforts at sub-micron scales [20,21], few studies focus on macro-scale, bulk material measurements [15,22], which are useful in continuum methods such as finite element analysis. Furthermore, the abovementioned efforts did not examine how such mechanics change during an animal's lifecycle.

In addition to the skin mechanical parameters, we also need to understand the propagation of mechanical cues to build a comprehensive biomechanical model of SAI afferents. The mechanical stimulus on the surface may appear in forms of pressure or skin deflection, and the interior deformations may be stress, strain or SED. There is a need to understand both: the native surface stimulus dictates our stimulus control selection during electrophysiological experiment, and the interior deformation impacts how we build computational neural models. So far, no agreement has been reached in either cue. On the surface, we would control force or displacement in case of pressure or deflection is the native cue, and in reality both controls were widely used [7,23]. A

review of the literature reveals that psychophysical experiments generally use force control, whether considering grating orientation [24] sphere size [25], or spatial anisotropy [26]. Interior of skin, modelers have used all stresses [27], strains [28] or SEDs [11] to predict neural firing, and their selection is mainly dependent on how well the model fit to one specific set of data. For example, an exhaustive survey of 28 candidate interior deformations were done to compare goodness of fits to SAI and RA recording data [27] and found that 15 of them fitted well. The drawback of this approach is that the selection is sensitive to the specific dataset and model used, and only gives empirical justification rather than theoretical explanation. To understand the exact propagation of these mechanical stimulus, we need to consider how one transformation from skin surface to its interior is superior to another, which we may find while observing how skin remodels.

Finally, this study seeks to understand sources of inter-fiber variability of SAI afferents. While SAI afferents are known to be highly variable between fibers [29], the source of such variability are not yet fully understood. One might speculate that may be due to skin mechanics, neural dynamics, and experiment artifacts. One aspect of the neural dynamics that we studied in the past is the end-organ architecture, that different groupings of the Merkel cell neurite-complexes may introduce differences in neural sensitivities [7]. It is not clear how this factor compares to others such as skin mechanics. While experimental control of skin mechanics is difficult, we can use computational modeling to analyze the contribution of the latter.

3 Aim I: Characterization of skin viscoelasticity

3.1 Introduction

The skin plays a critical role in protecting the musculoskeletal system and internal organs and serves to detect external stimuli. The skin's mechanical properties greatly impact how these functions are performed. Understanding these properties is essential for many applications, including functional tissue engineering [30]; however a full characterization of skin mechanical properties has not been accomplished due to its structural complexity. Skin consists of a multilayered epidermis and dermis [31] tied together by undulating interfaces embedded with pegged rete ridges. Each layer is different in both structure and function. For example, the outer stratum corneum of the epidermis is dry enucleated tissue that is stiffer the than remaining four layers of epidermis and serves as a physical barrier to the external environment. The dermis is made up of an extracellular matrix that includes collagen, elastin, and proteoglycans, among other components. Whereas the collagen and elastin fibers well account for the skin's mechanical behavior under tensile loading [16,17], further work suggests the filler substance of proteoglycans between cells may dictate the skin's behavior under compressive loading [32].

The skin's mechanical properties, especially viscoelastic relaxation, have been studied routinely in tension [1,16–19] but much less in compression, where they are likely to differ significantly. In addition, despite prior efforts at sub-micron scales [20,21], few studies focus on macro-scale, bulk material measurements [15,22], which are useful in continuum methods such as finite element analysis.

One open question is to what extent individual differences impact the range of skin relaxation (e.g., time constants and residual stress ratios). For example, individuals display a wide range of variability in skin properties at different body sites and during aging [13,33]. While only single-specimen experiments have been performed in compression [22], multiple-specimen results from skin in tension shed some light on this question. For example, investigations with a twistometer indicate that human skin thickness decreases after about 20 years of age [34] and aging speeds up skin relaxation [14]. In mice, skin relaxation in tension also depends on animal age and body site [14,35]. Therefore, while we know both animal age and body site correlate with thickness [15], we do not understand how variability in thickness influences the relaxation of the skin under compression. The skin's relaxation, and its variance between individuals, may impact somatosensory neural responses underlying the sense of touch [36], and thus is important for designing haptic devices to robustly and consistently deliver stimuli to the fingertip.

Beyond natural individual differences, biological material relaxation can be influenced by strain level and rate. Our understanding of such factors are vital to deciphering how we secure objects that are slipping from our grasp, for example [37]. Under tensile loading, Lanir has identified skin viscoelasticity to be strain-level dependent, where relaxation periods are elongated under larger strain [17,38]. Along the same lines, measurements of ankle ligaments indicate that the residual stress ratio decreases under larger strain [39]. Strain rates can significantly affect viscoelastic measurements as well. As shown for both articular cartilage [40] and human knee ligament [41], greater strain rates lead to greater peak forces.

In summary, the existing literature does not sufficiently describe the viscoelasticity of the skin, especially 1) in compression and 2) across a population of specimens with natural, individual differences, and 3) where strain level and rate can influence the results. The present study addresses these gaps in conducting compressive uniaxial tests on freshly excised mouse skin. Mouse skin was used because its thickness can be controlled through genetics, housing conditions and diet. The mouse is also the most widely used mammalian model system. To achieve different thicknesses, we sampled specimens from animals varying in age, hair cycle, body weight and skin site [15]. Specifically, the data were analyzed to determine if variability in skin thickness, as well as strain level and rate, contribute to variability in viscoelastic relaxation, as measured by relaxation time and steady-state residual stress ratio.

3.2   Materials and methods

3.2.1   Overall

Uniaxial compression experiments on flat, cylindrically cut skin samples utilized controlled displacement ramped into the skin surface to collect time-force displacement data. For the purposes of analyzing the data, we generated material parameters of the quasi-linear viscoelasticity (QLV) model [42]. To decouple viscoelasticity from other factors such as material hyperelasticity and stimuli conditions, we obtain QLV parameters from a hyper-viscoelastic constitutive model and only examined its viscoelastic parameters, rather than comparing the force traces alone. The measured specimens were from 139 skin samples freshly excised from 36 mice, ranging 5.7 – 34.3 weeks in age, and from three skin sites on the hindlimb: distal (Distal), proximal on nerve trunk (NT), and off nerve trunk (OffNT). The three skin sites were selected due to differences in their thickness and underlying fascial structures [15].

Three independent variables were examined for their correlation with skin viscoelasticity: skin thickness (range from 211 to 671 μm, natural variation due to hair cycles over selected age), strain level (steady-state stretch λ_∞ from about 0.2 to 0.8), and strain rate (median values of 0.06, 3.54 and 22.88 s^{-1}). Strain level is defined as $\varepsilon = |\ln(\lambda)| = -\ln(\lambda)$ in uniaxial compression, where ε denotes strain, λ denotes the stretch of material calculated from deformed thickness l divided by original thickness l_0, $\lambda = \frac{l}{l_0}$. The strain level dependency was analyzed using stretch, which aligns with finite deformation theory [43] and negatively correlates with strain level in the case of compression. The rate of strain was defined as $\dot{\varepsilon} = \frac{d\varepsilon}{dt}$.

Finally, to validate that the viscoelastic parameters obtained in the skin compression experiments could be used to predict the behavior of the skin in a different context, we performed a secondary experiment with fresh mouse skin where we changed the stimulus, specimen size and different boundary condition. Finite element analysis was used to predict the results of this experiment.

3.2.2 Ethics Statement

All animal use was conducted according to the National Institutes of Health *Guide for the Care and Use of Laboratory Animals* and was approved by the Institutional Animal Care and Use Committee of Columbia University (protocol AC-AAAC1561).

3.2.3 Apparatus

Compression tests were conducted on a custom-built test machine (Figure 3.1A), described in depth elsewhere [15]. Briefly, the test machine's components include a platen of aluminum (3 mm thick and 2.54 cm dia.) attached to a vertical load sled, which was driven by a motion controller (motion controller: Newport, Model ESP300, Mountain View, CA; linear stage: Newport, Model ILS100. Reaction force at the platen was measured by a loadcell (Honeywell, Miniature Model 31, Columbus, OH) with full capacity of 2.45 N mounted between the platen and vertical load sled, and its position was tracked by a laser displacement sensor (optoNCDT Model ILD 1402, Micro-Epsilon, Raleigh, NC) with a resolution of 1 μm. Both force and displacement were sampled at 1 kHz. The platen compressed the skin specimens against a rigid platform parallel to its surface, with sides of the cylindrical skin unconfined. The apparatus was equipped with a closed-loop control system integrated to maintain temperature of 32 degrees Celsius, consistent with prior works [6], using a BASIC Stamp microcontroller (Parallax Inc., Rocklin, CA) and associated electronic transistors and heating elements.
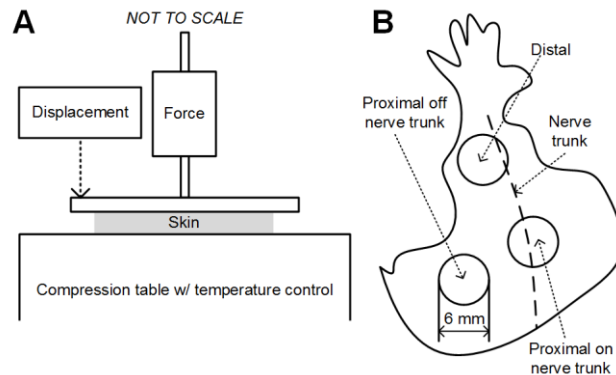
Figure 3.1 Schematic of the experiment apparatus for uniaxial unconfined compression tests. B: Schematic for locations of the excised skin site on mouse.

3.2.4 Animals and dissection

The animal preparation and dissection protocol has been described previously [15]. Skin samples were obtained using a 6-mm diameter punch (Acuderm Inc., Ft. Lauderdale, FL) after skin specimens were dissected from the mouse hindlimb. Three sampling sites (Figure 3.1B) were chosen at distal end of the hindlimb (Distal), and the proximal end of the hindlimb both off (OffNT) and on (NT) the saphenous nerve trunk because these sites appear to be categorically differentiable in terms of thickness. Specimens were harvested from a total of 36 mice, at ages ranging from 5.7 weeks to 34.3 weeks and body weights ranging from 15.9 grams to 61.4 grams. A total of 139 skin samples including 46 from Distal, 46 from OffNT and 47 from NT areas were harvested.

3.2.5 Skin test procedure

For all specimens, we first set the starting position of the platen to ensure it was positioned above the flat skin surface by observing the reaction force. Next, displacement-controlled compression was applied with a ramp-up phase at a velocity to achieve the desired strain rate, a hold phase at the maximum load position for 6 seconds (note that only the first 5 seconds were used in analysis to avoid analyzing the ramp-off response), and an unloading phase of the same rate as the ramp-up. Multiple repetitions of same loading protocol were applied to the specimen, where the 6th run for each skin specimen was analyzed and the first 5 repetitions were used as pre-conditioning to minimize the variance due to stress history [23].

Figure 3.2 demonstrates a typical experimental procedure, where strain rates are varied. Synthetic interstitial fluid (SIF) [44] was added via eye dropper to prevent drying of the skin. The

reaction force at the platen was measured by a loadcell and platen position measured by a laser displacement sensor. The recorded force trace was then used to determine the point of contact (Figure 3.2C). A "light-contact point" of the platen to the specimen surface was determined at the moment when reaction force on the platen exceeded 0.1 N. After that, the "contact point" was defined as distance from the platen to the rigid table at the "light-contact point", timed by a correction coefficient of 1.3. Then, the specimen thickness (l_0) and deformed thickness (l) was each defined as the distance from the platen to the rigid table at and after the "contact point".
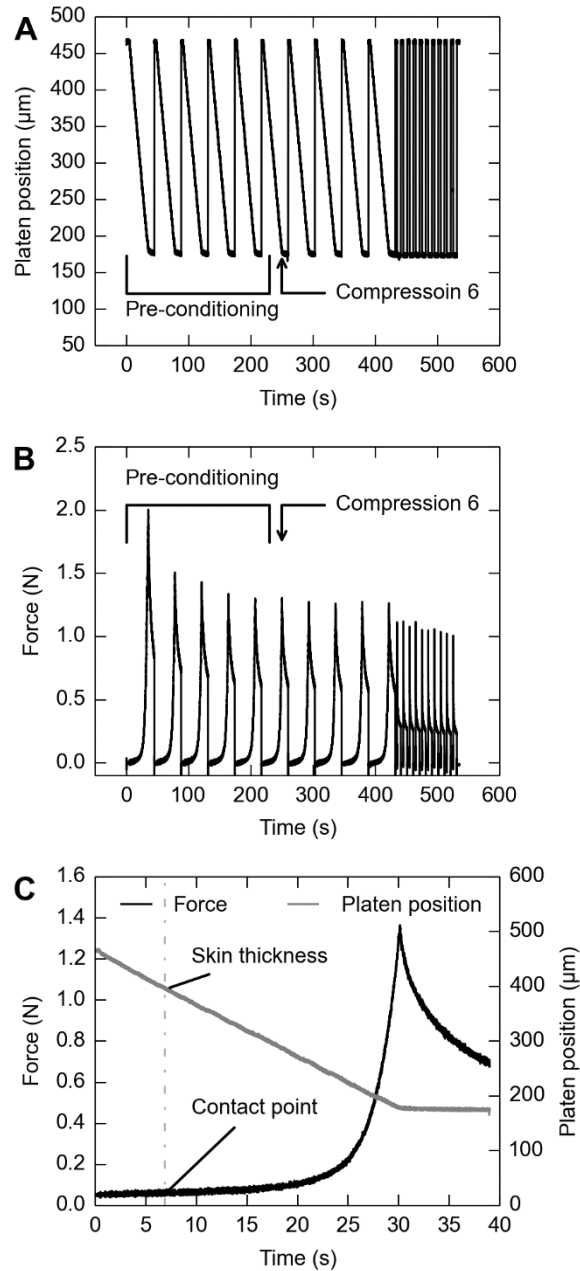
Figure 3.2 Example run of the compressive test procedure for one skin specimen when varying strain rates. A: Position of the compression platen over time, as measured by its distance from the fixed platform and B: reaction force at the compression platen. C: zoomed-in view of reaction force and platen position of Compression 6, demonstrating that "skin thickness" was defined by "contact point" determined from the force trace. The platen was moved into the skin with an acceleration of 0.06 s⁻¹ for each of the first 10 repetitions. Then, 10 additional compressions were performed at 22.88 s⁻¹. The 6th compression was analyzed in each sequence of 10 compressions.

Three different experimental paradigms were used to elucidate viscoelastic properties of multiple skin samples under compression. First, we measured skin under the same level of strain from 44 skin samples of naturally varying thickness. Maximum indentation depths were determined by manually searching for an instantaneous reaction force around 2 N, which is the approximate magnitude to generate a level of stretch of 0.6, similar to indentation in neurophysiological studies [6]. The velocity of the compression platen was 1 mm/s to achieve a strain rate of about 3.54 s^{-1}. Second, we applied similar procedures to 41 skin samples, but linearly varied steady-state stretch for each specimen. The minimum stretch level was set when the responsive force recorded at the loadcell was above zero, determined by its magnitude being one standard deviation above background noise, and the maximum stretch level was set when the maximum responsive force reached 2.45 N. Any force above this level was avoided to prevent damage to the skin or instrumentation. Figure 3.3 demonstrates the difference in stretch level between the first and second experimental paradigms. In the third experiment, strain rate was varied. Two rates (medians are 0.06 and 22.88 s^{-1}) were applied to 54 specimens, and the data were analyzed together with the first experiment (3.54 s^{-1}) to constitute three strain rates at different orders of magnitude. The low strain rate ($\dot{\varepsilon} = 0.06\ s^{-1}$) is comparable to activities with long relaxation times, such as standing and lying in bed, where one can still perceive the mattress even after several minutes. The medium strain rate ($\dot{\varepsilon} = 3.54\ s^{-1}$) corresponds to typical light-touch activities, such as typing on a keyboard. The high strain rate ($\dot{\varepsilon} = 22.88\ s^{-1}$) corresponds to impact loading, which one perceives to avoid imminent danger. The three strain rates correspond to 0.01, 1 mm/s and the fastest moving velocity of our test machine.
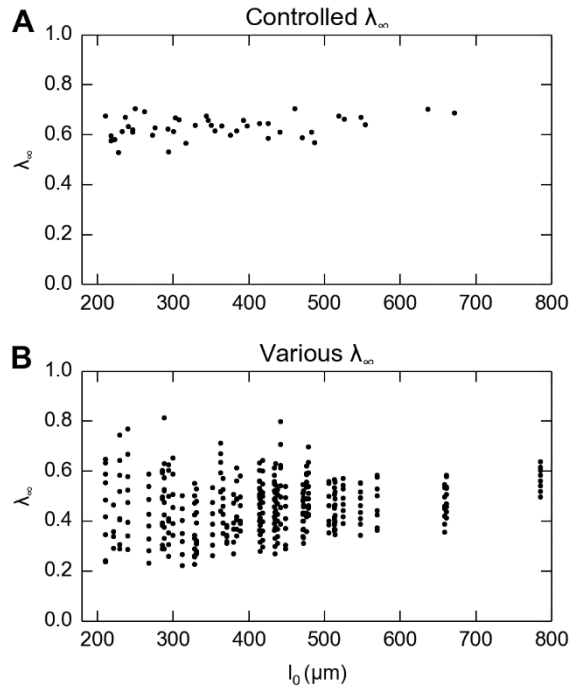
Figure 3.3 There is no correlation between the measured steady-state stretch (λ_∞) and thickness. A: Skin thickness naturally varies between about 200 and 800 μm when a single, consistent stretch level of about 0.6 is delivered to each specimen in the first experiment. B: Skin thickness naturally varies when multiple stretch levels (λ_∞ from about 0.2 to 0.8) are delivered to each of the skin specimens.

3.2.6   Constitutive laws

Hyper- and visco-elastic models have been adopted to fit the behavior of the experimental data, as previous efforts [22] have shown that skin under compression is hyper-viscoelastic. On a macro-scale, most biological tissues are viscoelastic [42] and have well-developed material models depending on the deformation level. Under small deformation, various spring-dashpot models have been used, including the most commonly used Kelvin-Voigt model, a standard linear solid model and generalized Maxwell model (i.e., Maxwell-Wiechert model) [45]. As biological tissue often undergoes finite deformation, these linear models must be modified to incorporate hyperelastic components. Two of the most popular models are the quasi-linear viscoelastic (QLV)

model [42] and parallel-network viscoelastic (PNV) model [46]. Although the PNV model yields

accurate and stable strain-energy outputs, the QLV model is more popular because the

parameters are typically easier to interpret and it has a longer history (Figure 3.4).
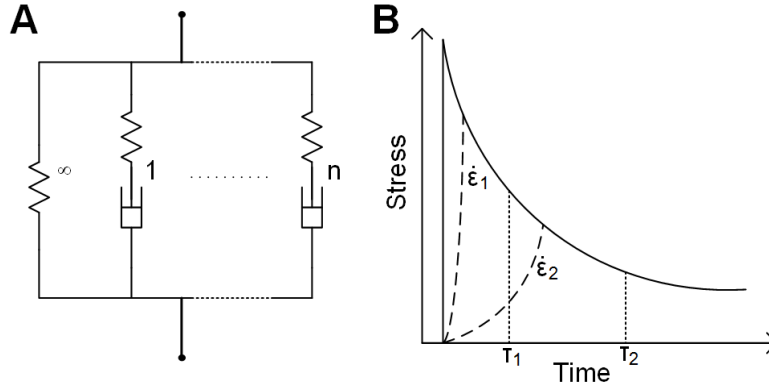
Figure 3.4 A: Schematic of the QLV model, where the material consists of parallel chains, and each chain consists of an elastic component (denoted by a spring) and a viscous component (denoted by a dashpot). Usually, the steady-state response of a viscoelastic solid is represented by a chain with no viscous component (i.e., $\tau = \infty$). Here, in addition to one solid chain, models including one and two chains with viscous components are evaluated and denoted as the one-term and two-term models. B: Illustration of how stimuli with a low strain-rate may lose information from low time-constant QLV chains. The solid line is the response of a typical two-term viscoelastic solid with time constants τ_1 and τ_2 under a step load. Two dashed lines represent the response of the material under slower strain-rates. For the slowest strain-rate, $\dot{\varepsilon}_2$, stress relaxation properties of the faster chain (τ_1) may not show up because its relaxation for the faster chain takes place within its ramp phase. Therefore this will not captured by a curve fitting, which simply characterizes the material as a one-term QLV solid and only calculates the slower chain (with time constant τ_2). Thus, we can eliminate the two extra parameters (G_1, τ_1) if we only care about low strain-rate situations. In other words, for low strain-rate cases, the single term model is sufficient and therefore more appropriate than the two-term models because of the reduced number of free parameters.

For the QLV model, a convolution integral was used to calculate stress from strain data,

$$\sigma(t) = \int_{-\infty}^{t} G(t - t') \frac{\partial \sigma_e(\lambda)}{\partial \lambda} \frac{\partial \lambda(t')}{\partial t'} dt' \qquad (3.1)$$

where t and λ denote time and stretch at any given moment t. The instantaneous elastic function of material is $\sigma_e(\lambda)$, where herein we utilized a 1st-order Ogden form of the hyperelastic strain energy function [47],

$$\sigma_e(\lambda) = \frac{2\mu}{\alpha}(\lambda^\alpha - \lambda^{-\frac{\alpha}{2}}) \qquad (3.2)$$

with μ and α being the material constants, μ also known as instantaneous elastic modulus. $G(t)$ is defined as the reduced relaxation function, and is in the form of a Prony series,

$$G(t) = \sum_{i=1}^{n} G_i e^{-\frac{t}{\tau_i}} + G_\infty \qquad (3.3)$$

where τ_i were the time constants associated with stress relaxation ratio G_i, and G_∞ was the residual stress ratio at the steady state. At time $t = 0$ the value of $G(t)$ was defined as unity.

$$\sum_{i=1}^{n} G_i + G_\infty = 1 \qquad (3.4)$$

The QLV models presented here include an Ogden elastic representation and a Prony series relaxation function utilizing one and two terms, (where $n = 1$ and $n = 2$ specifically), that were referred to as "one-term QLV" and "two-term QLV", respectively. There are 2 independent viscoelastic parameters for the one-term model (τ_1, G_∞; note that $G_1 = 1 - G_\infty$ and therefore is not independent) and 4 for the two-term model ($\tau_1, \tau_2, G_1, G_\infty$) as shown in Equation (3.5) and (3.6), not counting the two hyperelastic parameters (μ, α). Since the one-term model had fewer free variables (at the cost of inability to predict response for high strain-rates, Figure 3.4B) it was therefore preferred given similar goodness of fit to the two-term model.

$$G(t) = G_1 e^{-\frac{t}{\tau_1}} + G_\infty \qquad (3.5)$$

$$G(t) = G_1 e^{-\frac{t}{\tau_1}} + G_2 e^{-\frac{t}{\tau_2}} + G_\infty \qquad (3.6)$$

In contrast to the previous recursive method [48], the implemented numerical algorithm is designed to be in vector form so for-loops can be avoided, thus it is much easier to implement in numerical packages like MATLAB and NumPy. We first start from Equation (3.1), which can be split by applying Equation (3.3),

$$\sigma(t) = \sum_{i=1}^{n} \sigma_i(t) + \sigma_\infty(t) \qquad (3.7)$$

Where

$$\sigma_i(t) = \int_{-\infty}^{t} G_i e^{-\frac{t-t'}{\tau_i}} \frac{\partial \sigma_e(\lambda)}{\partial \lambda} \frac{\partial \lambda(t')}{\partial t'} dt' \qquad (3.8)$$

$$\sigma_\infty(t) = \int_{-\infty}^{t} G_\infty \frac{\partial \sigma_e(\lambda)}{\partial \lambda} \frac{\partial \lambda(t')}{\partial t'} dt' \qquad (3.9)$$

By assuming no stress history before $t = 0$ and identifying the constants in Equation (3.8), we have

$$\sigma_i(t) = G_i e^{-\frac{t}{\tau_i}} \int_{0}^{t} e^{\frac{t'}{\tau_i}} \frac{\partial \sigma_e(\lambda)}{\partial \lambda} \frac{\partial \lambda(t')}{\partial t'} dt' \qquad (3.10)$$

And this is now ready for numerical implementation, as

$$\sigma_i^k = G_i e^{-\frac{t^k}{\tau_i}} \sum_{l=2}^{k} e^{\frac{t^l}{\tau_i}} (\sigma_e^l - \sigma_e^{l-1}) \qquad (3.11)$$

where the superscript k means the value at kth point in time, i.e., σ^k means stress at time t^k. The summation starts from $l = 2$ because we assert the stress change is zero at time zero. Also, from Equation (3.2) we calculate instantaneous stress as

$$\sigma_e^k = \frac{2\mu}{\alpha}[(\lambda^k)^\alpha - (\lambda^k)^{-\frac{\alpha}{2}}] \qquad (3.12)$$

Similarly, we can obtain

$$\sigma_\infty^k = G_\infty \sum_{l=2}^{k}(\sigma_e^l - \sigma_e^{l-1}) \qquad (3.13)$$

And the final stress evolution can be computed from

$$\sigma^k = \sum_{i=1}^{n}\sigma_i^k + \sigma_\infty^k \qquad (3.14)$$

Thus Equation (3.11) − (3.14) completes the numerical implementation of QLV model.

3.2.7 Fitting experimental data to constitutive model

To attain the parameters of the constitutive model, we fit the model to the stress-stretch-time curves calculated from the experimental data. The stretch value was calculated by dividing deformed thickness l over original thickness l_0, i.e. $\lambda = \frac{l}{l_0}$ (l, l_0 defined in Section 2.4). Recorded experimental force data were converted to stress values by dividing force over area, calculated from (3.15), with the assumption that the volume of the specimen remained constant because it is nearly incompressible [42]:

$$A = \frac{A_0}{\lambda} \qquad (3.15)$$

where A_0 is the area of the punch, a 6-mm diameter circle. For the detailed numerical algorithm used for fitting, please refer to the Appendix I. QLV model parameters were then adjusted to fit to the stress-time and stretch-time measurements (Figure 3.5) taking the number of terms $n = 1$ and $n = 2$.
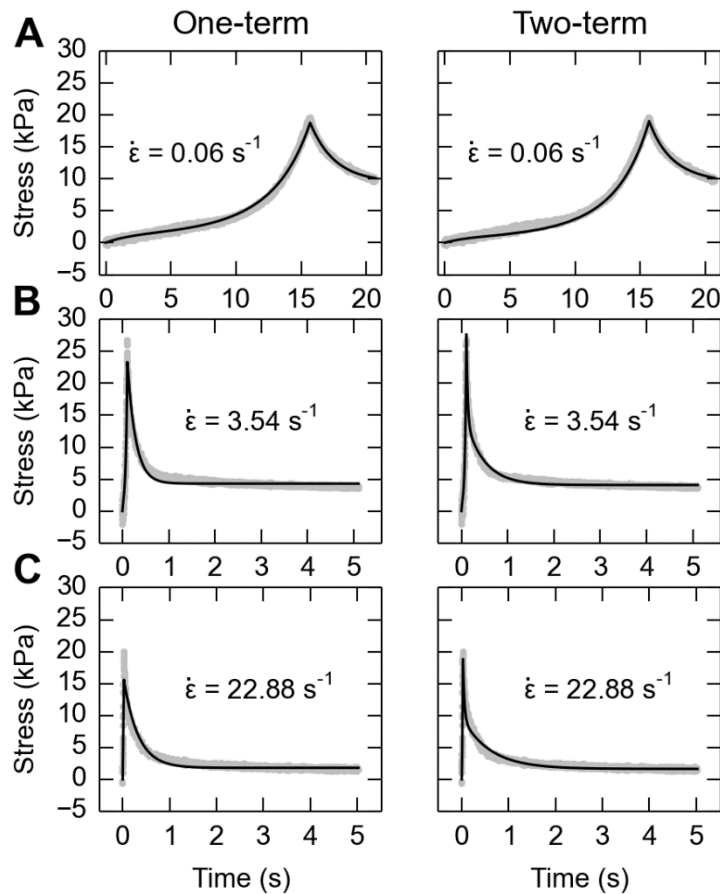
Figure 3.5 Example fit of stress over time by one-term (left column) and two-term (right column) QLV models at three strain rates (rows A: 0.06 s^{-1}; B: 4.29 s^{-1}; C: 35.34 s^{-1}). Black line shows the modeled prediction, and grey data points show the experimental data. The average weighted R^2 value for the one-term case for the three strain-rates is 0.86 while the R^2 value using the two-term case is 0.93. Therefore, the tradeoff is number of free parameters increased from 1 to 2, vs. attaining a slight improvement to the fitting, and herein we chose the one-term case for this reason.

The stress and stretch history over the whole time window, including phases of both the ramp (from contact to peak stress) and hold (from peak stress to 5 seconds after), were used in the fitting to account for relaxation during loading, similar to Laksari et al. [49]. Because the number of data points in the hold phase were much greater than that in ramp phase, we used an R^2 value

as the equally-weighted sum between the R^2 from fit of the ramp phase and hold phase. For each specimen, the weighted R^2 was maximized through a constrained nonlinear optimization (fmincon, in the MATLAB Optimization Toolbox) using the SQP algorithm. The reduced chi-square value (χ^2_{red}) and the residual standard deviations (σ_{res}) were also checked to assure the quality of fit.

Then, fitting of both one- and two-term models was performed in two steps:

1) We fit the experimental data with all free viscoelastic parameters (2 and 4 for one- and two-term models, respectively) and all free hyperelastic parameters (2 for each model), with manually chosen initial values for the optimization algorithm.

2) We fixed all time constant parameters (τ) and initial shear modulus (μ) to median values found in Step 1 between specimens tested under same strain rate. For the initial values for free parameters, corresponding median values found in Step 1 were used.

By fixing certain parameters in Step (2), the total number of free viscoelastic parameters were reduced to 1 for one-term (G_∞) and 2 for two-term models (G_1, G_∞) respectively, and also included only 1 hyperelastic parameter (α) in each. For analysis of the distribution of time constants (τ), fitting results from Step 1 were used, and for that of stress ratios (G) results from Step 2 were used.

The fitting of QLV model to experiment data for each skin specimen was performed and results were listed in Table 3.1, which shows high R^2 values, χ^2_{res} close to 1 and low σ_{res} (< 1 kPa,

compared to peak stress of about 50 kPa in the 2nd experiment), indicating a good fit. Data in Table

3.1 and Figure 3.5 reveal the trade-off for increasing the number of free parameters from 1 to 2

was attaining only a small improvement in fit. Thus, we decided to use the one-term model so

that comparisons between specimens were easier with only a single free parameter. More

importantly, by strictly controlling the number of free parameters, we minimized the non-unicity

of the fitting.

Table 3.1 Median parameters from model fits to data for all experimental conditions

Experiment	$\dot{\varepsilon}\ (s^{-1})$	Model	Material parameters							Goodness of fit		
			$\tau_1(s)$	$\tau_2\ (s)$	G_1	G_2	G_∞	$\mu\ (kPa)$	α	R^2	χ^2_{red}	$\sigma_{res}\ (kPa)$
First	3.54	One-term	0.180	-	0.748	-	0.252	6.422	10.703	0.870	1.001	0.448
		Two-term	0.028	0.410	0.631	0.189	0.143	7.958	12.683	0.910	1.001	0.325
Second	1.47	One-term	0.236	-	0.548	-	0.452	7.189	7.924	0.921	1.001	0.904
		Two-term	0.092	1.111	0.482	0.110	0.351	6.354	8.787	0.958	1.002	0.735
Third	0.06	One-term	1.900	-	0.684	-	0.316	7.162	6.511	0.974	1.328	0.456
		Two-term	1.569	50.895	0.612	0.368	0.000	5.453	7.573	0.974	1.471	0.475
	22.88	One-term	0.310	-	0.666	-	0.334	4.057	3.447	0.816	1.004	0.381
		Two-term	0.030	0.599	0.608	0.212	0.195	3.973	6.624	0.951	1.001	0.175

3.2.8   Finite element analysis

To exclude the case where the frictional boundary conditions might confound the trend between

thickness, stretch levels and viscoelasticity, numerical experiments of finite element (FE) analysis

were performed using the commercial FE software package ABAQUS Standard, version 6.12 (Dassault Systèmes, Vélizy-Villacoublay, France).
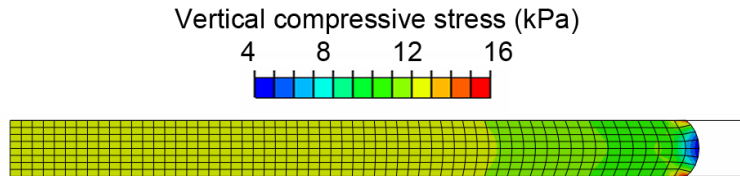
Figure 3.6 Typical distribution of vertical compressive stress (S22 in ABAQUS) from the axisymmetric FE simulation (therefore only the right half of the skin middle-section is shown), with friction coefficient of 0.3 and skin thickness of 400 μm. Note that there is only minor edge effect around the periphery.

Numerical experiments of skin specimens were performed using axisymmetric models (Figure 3.6), in which the geometry was the same as the biological specimen (6 mm dia. cylindrical skin piece). The material parameters assigned were from Table 3.1, using the two-term QLV model for higher accuracy. Three frictional coefficients (μ_f) between the skin and compression platen/table were tested, namely 0 (frictionless), 0.3 (between human finger and metal tip [50]), and ∞ (rough). The rough friction coefficient also accounts for the cohesive force between skin and the metal, given that our boundary condition enforces no separation after contact [51]. Contact behaviors were defined in both a) tangential behavior, where isotropic friction was specified with penalty friction formulation, and b) normal behavior, where "hard" contact pressure-overclosure was used. A high Poisson's ratio $\nu = 0.475$ for the skin were used. First, in line with the skin compression experiments, models of skin thickness from 200 to 800 μm with 100 μm increments were constructed. CAX4RH elements 50 μm in edge length were used. The stretch level and ramp time were both derived from the median values in the compression experiment where skin thickness

31

varied, namely $\lambda_\infty = 0.63$, $t_{ramp} = 0.129\ s$. The aforementioned model with skin thickness of 400 μm was then modified for a second experiment on variability in stretch level, where steady-state stretches were varied from 0.2 to 0.8 with an increment of 0.1. After the analyses were completed, the reaction force and displacement at the compression platen were extracted and processed in the same manner as the data from the skin compression experiments (described in Section 2.6), and the viscoelastic parameters were then compared to those obtained from the compression experiments.

3.2.9   Role of dermis-epidermis thickness ratio

In addition to the absolute thickness of a skin specimen, another independent variable that might contribute to viscoelastic variability is the relative thickness ratios between skin layers, as this changes between skin sites of Distal, OffNT and NT. The thickness ratios between dermis and epidermis, as previously obtained for different skin sites [15], were used as the independent variable here.

3.2.10 Validation experiment

An additional compression experiment with mouse skin was performed with a small ceramic tip of 1.5 mm diameter, using a larger skin specimen of 8 mm diameter, sampled from the right hind leg of a 9.4-week-old mouse. The skin specimen was placed on the aforementioned aluminum compression table with sufficient SIF to prevent skin from drying (Figure 3.7A). Four ramp and hold displacement-controlled indentations were commanded at 1 mm/s, i.e., two iterations at two magnitudes, which were chosen to achieve approximately $\lambda_\infty = 0.5$. Force-time data were

recorded, from which probe-to-skin contact points were determined when force crossed a threshold of 0.5 mN. The data were post-processed with Python packages of SciPy and NumPy.

To predict the result of this experiment using material model data from the flat plate experiments, a finite element analysis was performed in ABAQUS Standard. The model was constructed of approximately 800 CAX4RH elements (Figure 3.7B). The skin thickness was 225 µm, which is at the median for a 9-week-old mouse [15]. Four layers of equal-sized elements were specified in the thickness direction. One hundred single-biased elements were specified in the radial direction with a bias ratio of 5 and higher mesh density near the symmetric axis than the peripheral axis. The ceramic tip was modeled as 0.75 mm radius cylinder with fillet radius of 0.15 mm. The friction coefficient between the ceramic and skin was chosen as 0.3 [7], and 0 between the aluminum and skin. For all contact interactions, "hard" contact, pressure overclosures were used and no separation after contact was allowed. Material properties from the second experiment with the flat plate indenter were used, which employed the two-term model (4th line in Table 3.1).
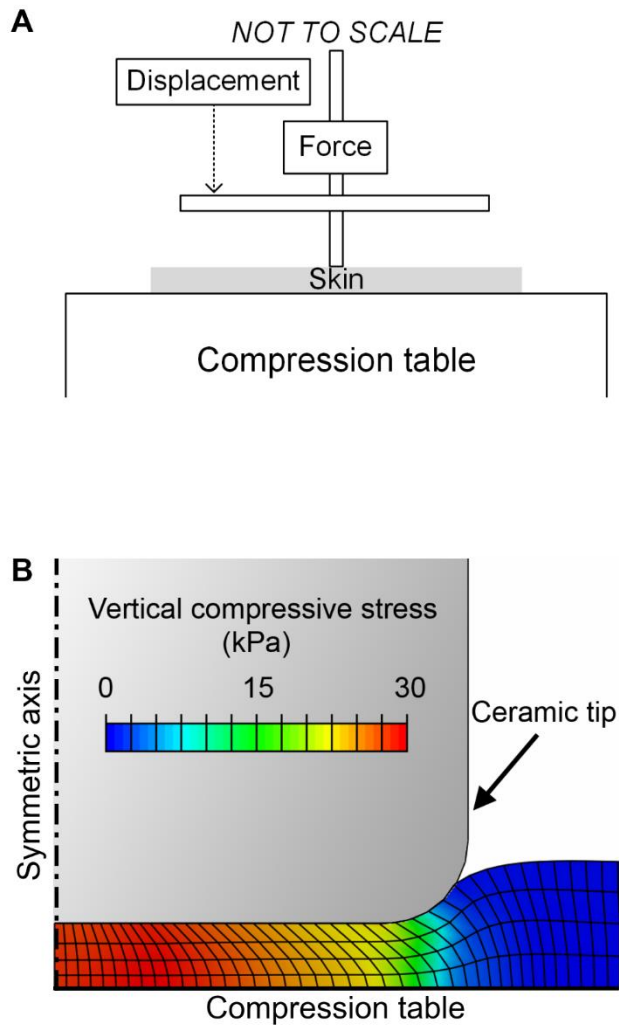
Figure 3.7 Validation experiment in a secondary context using a 1.5 mm tip and 8 mm skin specimen to demonstrate the applicability of the measured QLV parameters. A: Schematic drawing of experiment set-up; B: Finite element model zoomed-in to the contact region.

3.3 Results

The parameters returned by fitting the one-term QLV model revealed that skin viscoelasticity is highly variable between specimens, yet correlates with the three independent variables. Specifically, the residual stress ratio G_∞ positively correlates with skin thickness and stretch level, and the time constant τ_1 negatively correlates with strain rate.

3.3.1 Large variability between specimens

Large variability was observed from all three independent variables. First, as between specimen thickness changed from 211 to 671 μm, we observed significant variation in both QLV parameters: the relaxation time constant ($\tau_1 = 0.19 \pm 0.10\ s$) and the steady-state residual stress ratio ($G_\infty = 0.28 \pm 0.13$). Second, as skin thickness naturally varied (Figure 3.8A) and steady-state stretch was increased (λ_∞ from 0.22 to 0.81, Figure 3.8B), we observed significant variation in both QLV parameters ($\tau_1 = 0.26 \pm 0.14\ s$, Figure 3.8C; $G_\infty = 0.47 \pm 0.17$, Figure 3.8D). Third, as strain rate was increased from 0.06 to 22.88 s^{-1}, the median time constant τ_1 varied from 1.90 to 0.31 s.
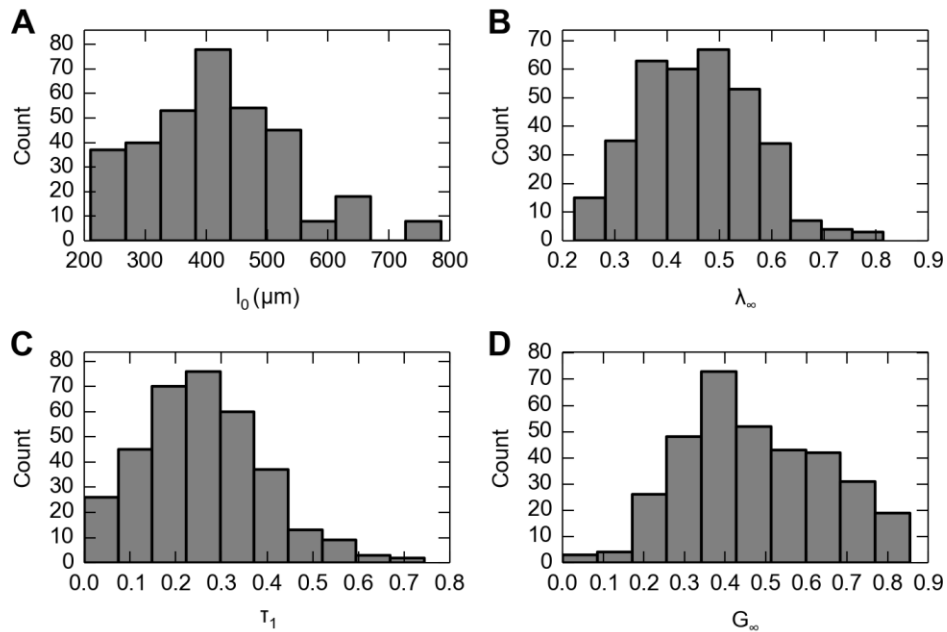
Figure 3.8 Data from 341 experimental runs (n=41 specimens) each stimulated an average of eight stretch levels. Distributions are shown of A: skin thickness measurements; B: steady-state skin stretches (λ_∞) applied; C: time constants from fitting stress versus time to the one-term QLV model; D: the steady-state residual stress ratio G_∞. Note that each of the four variables exhibits high variability.

3.3.2 Positive correlation between thickness and residual stress ratio

In the first experiment where the skin thickness naturally varied, residual stress ratio G_∞ positively correlated with skin thickness, with Pearson correlation coefficient of 0.883 (Figure 3.9A). Linear regression with residual stress ratio G_∞ as a dependent variable was performed, which returned $p < 0.001$ for independent variable thickness l_0, and $G_\infty = 9.997 \times 10^{-4} \mu m^{-1} \cdot l_0 + 0.077$.
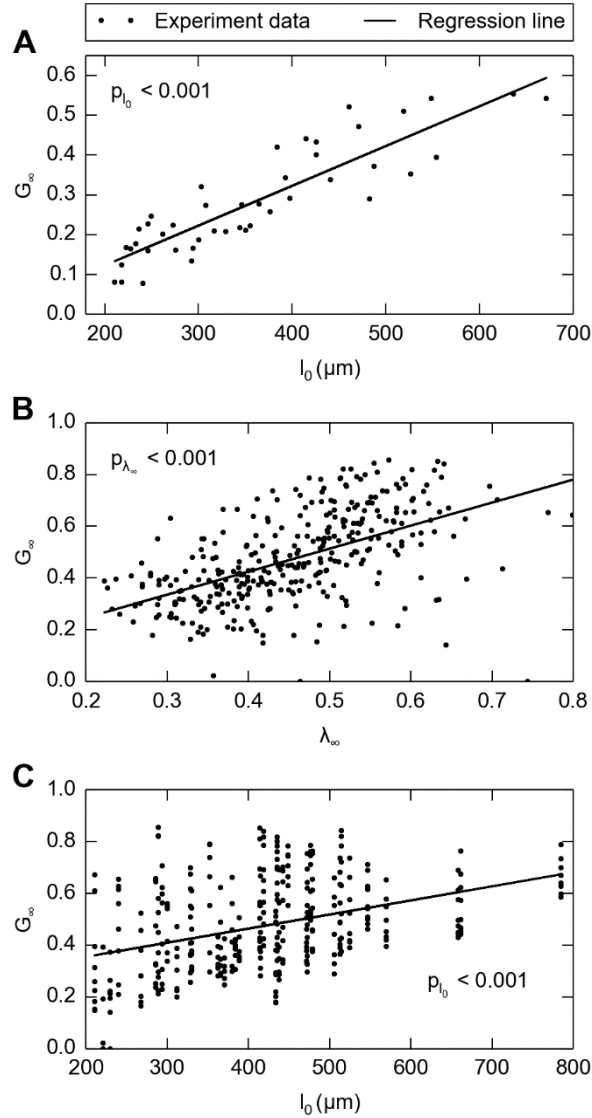
Figure 3.9 A: In the first experiment where only thickness varied, the steady-state residual stress ratio (G_∞) correlates with increasing skin thickness, n=44. Linear regression (solid line) with residual stress ratio G_∞ as the dependent variable was performed, which returns $p < 0.001$ for independent variable thickness l_0, and $G_\infty = 9.997 \times 10^{-4} \mu m^{-1} \cdot l_0 + 0.077$. In the second experiment where both thickness and strain level varied, the residual stress ratio (G_∞) correlates with both B: stretch and C: skin thickness. Note that the two correlations are independent from each other because there is no correlation between stretch and skin thickness. Multilinear regression with residual stress ratio G_∞ was also performed, which returns $p < 0.001$ for independent variable stretch λ_∞, $p < 0.001$ for independent variable thickness l_0, and $G_\infty = 0.810 \cdot \lambda_\infty + 4.25 \times 10^{-4} \mu m^{-1} \cdot l_0 - 0.074$. Note that in B and C, solid lines are single-linear regressions for residual stress ratio with respect to stretch and thickness respectively.

3.3.3 Strain-level dependency

In the second experiment where the change in stretch delivered accompanied skin thickness variation, the residual stress ratio G_∞ was found to positively correlate with skin thickness (Figure 3.9B), and moreover, also positively correlated with stretch level (Figure 3.9C). Multilinear regression with residual stress ratio G_∞ was also performed, which returns $p < 0.001$ for independent variable stretch λ_∞, $p < 0.001$ for independent variable thickness l_0, and $G_\infty = 0.810 \cdot \lambda_\infty + 4.25 \times 10^{-4} \mu\text{m}^{-1} \cdot l_0 - 0.074$, indicating that both skin thickness and stretch level are positively correlated with residual stress ratio and thus contribute to variability.

3.3.4 Strain-rate dependency

In the third experiment, the strain rate largely varied (median $\dot{\varepsilon} = 0.06, 22.88$) and combined with data from first experiment (median $\dot{\varepsilon} = 3.54$), we found that the same magnitude of relaxation takes place at significantly shorter time constants at higher strain rates (Figure 3.10A). Linear regression was performed with time constant τ_1 as the dependent variable and strain rate $\dot{\varepsilon}$ as the independent variable, which yielded a significantly negative correlation ($p < 0.001$) between the strain rate and time constant. Using the same regression but replacing the dependent variable from time constant τ_1 with residual stress ratio G_∞, we found that the strain rate did not significantly affect residual stress ratio ($p = 0.988 > 0.05$). With a closer examination of the distribution of time constants and residual stress ratios (Figure 3.10B-D), we noticed that the distributions of time constants notably skewed to the left as strain rate increased, whereas the distribution of residual stress ratios did not show systematic changes.
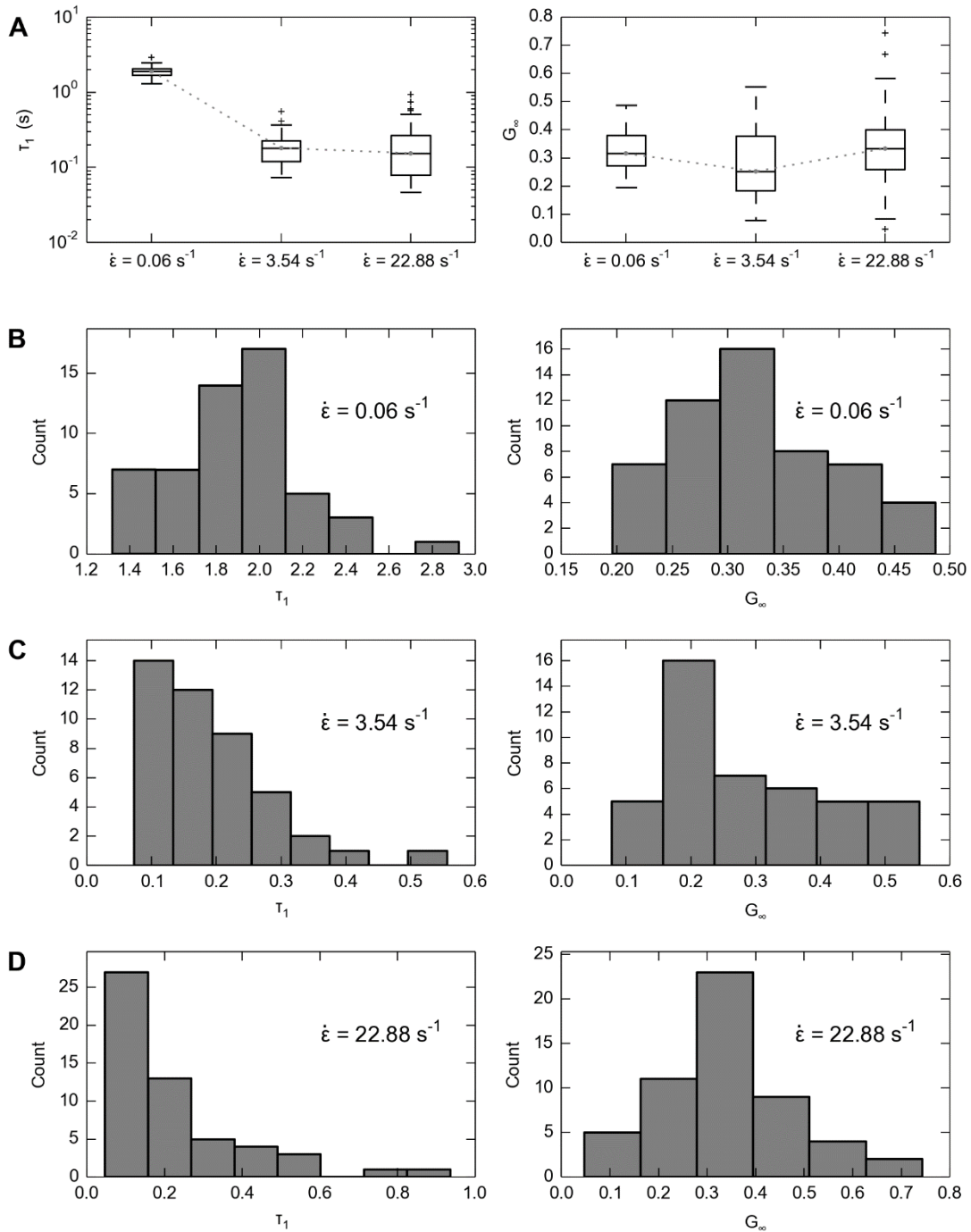
Figure 3.10 Values of time constant (τ_1) and residual stress ratio (G_∞) at three strain rates ($\dot{\varepsilon}$). A: Overall, the time constants are significantly smaller under faster strain rates, while there is no systematic trend in the change of residual stress ratio. The boxes range from the lower quartile to upper quartile, the centerlines denote the medians, the whiskers denote extreme values and crosses denote outliers. B-D: Detailed views of the distributions of time constants and residual

stress ratios from all data points at B: strain rate 0.06 s^{-1}, n = 54; C: strain rate 3.54 s^{-1}, n = 44; D: strain rate 22.88 s^{-1}, n = 54.

3.3.5   Finite element analysis

In Figure 3.11 we showed FE simulations on same skin thickness (400 µm) but under extreme frictional conditions (frictionless and rough), for different stimulus magnitudes (λ_∞ from 0.5 to 0.7). Reduced relaxation functions obtained from fitting the hyper-viscoelastic constitutive model was also plotted in Figure 3.11C. This shows that although changes in frictional conditions result in different force responses, the viscoelastic reduced relaxation functions are not impacted. The final outcome of the FE analysis, testing whether the effect of thickness on viscoelasticity is caused by frictional edge effects or the innate property of the skin, showed that the edge effect negligibly influences the outcome (Figure 3.12A), independent of three levels of friction coefficients. Similarly, the frictional edge effects negligibly influence the outcome caused by strain level as well (Figure 3.12B).
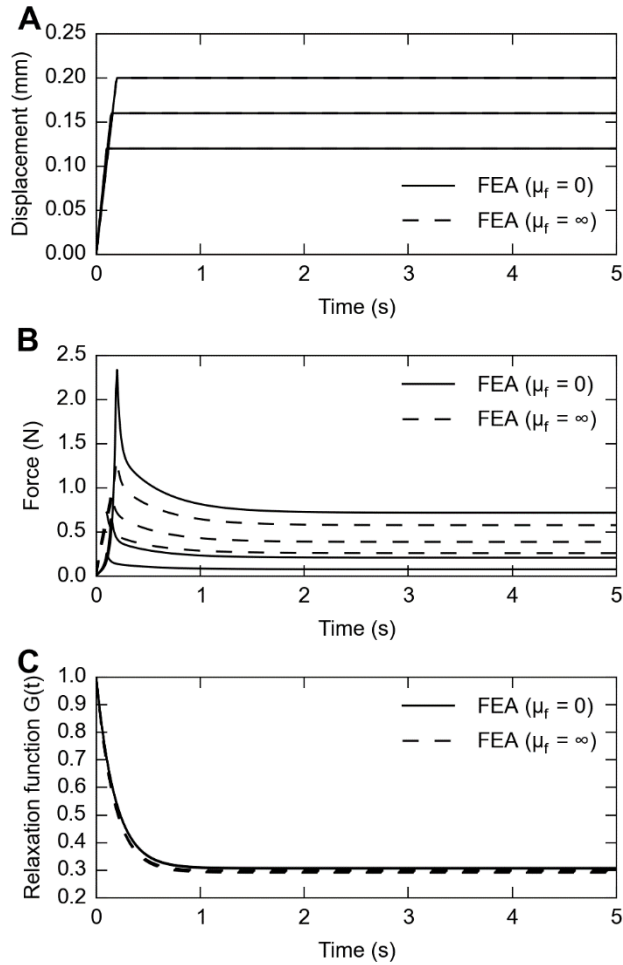
Figure 3.11 FE simulations for skin thickness of 400 μm, at stretch level of 0.5, 0.6 and 0.7, under frictionless (solid lines) and rough (dashed lines) friction conditions. A: displacement stimuli to achieve desired stretch level; B: responsive force traces for three stretch levels under different friction conditions; C: calculated relaxation function for force traces shown in B. Note that while friction conditions have an impact on responsive force traces, they do not impact the calculated viscoelastic reduced relaxation function.
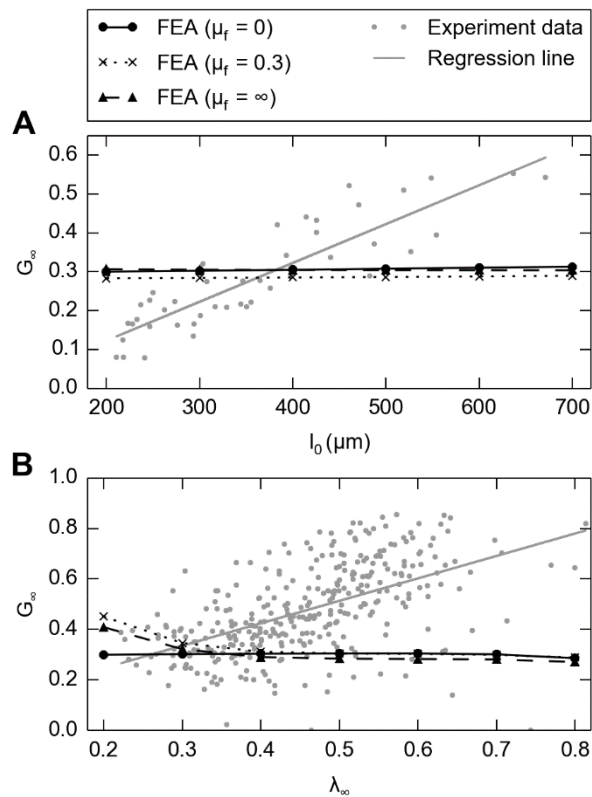
Figure 3.12 FE analysis shows minimal effect of frictional edge effects on calculated residual stress ratio, A: when skin thickness changes, plotted on top of Figure 3.9A; and B: when strain level changes, plotted on top of Figure 3.9B.

3.3.6   Role of dermis-epidermis thickness ratio

Value of this dermis-epidermis thickness ratio, denoted as r, is listed in Table 3.2. During the analysis of the first experiment when skin thickness varied, a multi-linear regression was performed with residual stress ratio G_∞ as the dependent variable, and returned $p < 0.001$ for the independent variable thickness l_0 but $p = 0.63 > 0.05$ for the independent variable dermis-epidermis thickness ratio r (Table 3.2). This indicates that the impact for the dermis-epidermis thickness ratio r was insignificant on residual stress ratio.

Table 3.2 Value of dermis/epidermis thickness ratio r previously measured [15]

	Epidermis			Dermis		
	Distal	OffNT	NT	Distal	OffNT	NT
Average thickness (pixels)	16.30	15.00	11.70	194.00	352.80	288.50
	13.70	14.00	13.50	228.30	239.80	378.00
	16.30	14.30	14.20	195.80	259.90	405.00
	15.80	14.20	13.70	311.80	563.20	471.80
	15.30	14.00	13.70	260.20	575.80	567.20
	17.80	15.80	13.00	308.50	555.20	575.50
	15.80	13.50	14.80	150.20	256.80	634.30
	16.80	13.80	15.70	126.80	216.50	478.80
	15.50	13.20	14.50	128.00	257.50	496.30
Mean	15.92	14.20	13.87	211.51	364.17	477.27
Std.	1.12	0.79	1.14	71.22	154.95	108.11
n	9	9	9	9	9	9
				Distal	OffNT	NT
Epidermis/dermis thickness ratio				13.28	25.65	34.42

3.3.7 Validation experiment

Good agreement was observed between the force-time curves from FE model prediction and from the experiment, with an average $R^2 = 0.932$ (Figure 3.13). A rapid decay at the early relaxation (< 1 s) was followed by one more gradual (1 – 5 s) and observed in both the experiment and the model prediction. The accurate prediction in this new context – given changes in skin size, indenter tip, and boundary conditions – demonstrates the applicability of QLV constitutive parameters presented herein, within the time window between 0 – 5 s.
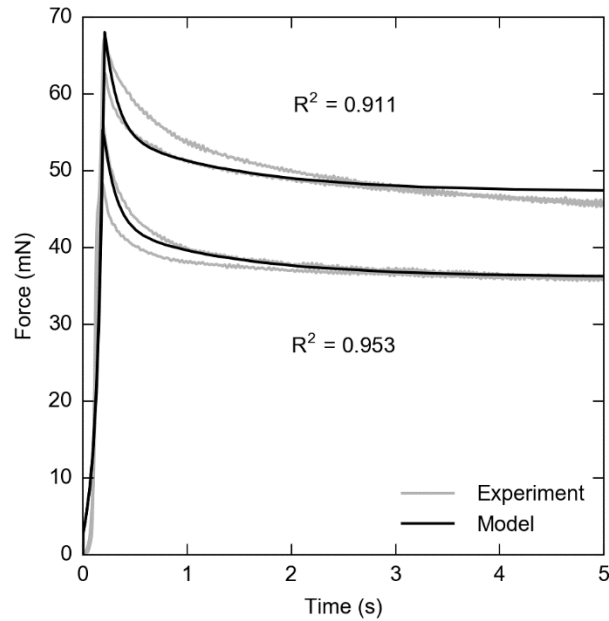
Figure 3.13 Validation result from FEA shows good agreement between numerical prediction and actual experiment measurement.

3.4   Discussion

This work shows, for the first time with mouse skin under compression, that skin's viscoelasticity is highly variable (relaxation time constant $\tau_1 = 0.19 \pm 0.10\ s$ and steady-state residual stress ratio $G_\infty = 0.28 \pm 0.13$) among a population of skin specimens ($n = 139$). However, we found systematic correlation in three cases: 1) the residual stress ratio G_∞ positively correlates with skin thickness (p < 0.001), 2) residual stress ratio positively correlates with stretch level (p < 0.001), in other words, negatively correlates with strain level and 3) the time constant τ_1 negatively correlates strain rate ($p < 0.001$). Overall, these findings shed light on the natural range of between-specimen variance under compression, and reveal how experimental controls of strain level and rate can influence measurement of the same specimen.

A small, secondary experiment with fresh mouse skin was performed to validate that the viscoelastic parameters obtained in the skin compression experiments could be used to predict the behavior of the skin in a different context. In particular, using the viscoelastic parameters obtained with the flat plate, we sought to predict the force relaxation of a 1.5 mm probe indented into a skin specimen of different cut-out size (8 mm as opposed to 6 mm), for two indentation depths. This required a compression experiment with mouse skin, as well the use of a finite element model. As denoted in Appendix IV, the force relaxation predicted by the FE model well agrees with experimental data, with an average $R^2 = 0.932$.

We found that as thickness decreases, residual stress ratio decreases, which means the skin relaxes to a greater extent. This finding agrees with a study by Escoffier et. al [14], who reported that relaxation time decreases as people age, and we know that skin thickness decreases with aging [34]. Also, we identified that the residual stress ratio decreases with lower levels of stretch, i.e., higher strain levels, which echoes Funk et. al [39] who reported the same effect in ankle ligaments. The work herein is the first to report a decrease in time constant under a faster strain rate from biological measurements.

Although the dependency of the skin's mechanical properties on strain and strain-rate is constitutively defined as material non-linearity, the dependency on skin thickness indicates that skin specimens of varying thickness are essentially different materials. Additional analyses indicate that the dependency of skin viscoelasticity on thickness and strain level are neither from frictional edge effects (computational finite element analysis, Appendix II) nor from different dermis-epidermis thickness ratios (statistical regression, Appendix III).

Our results from mouse hindlimb skin are comparable to prior tests of compression with pig dorsal skin [22], exhibiting similar time constants within a 5-second time-scale (median $\tau_1 = 0.18\ s$ from our one-term model fit compared to $\tau_1 = 0.57\ s$ on pig skin) and residual stress ratios (median $G_\infty = 0.284$ herein, compared to $G_\infty = 0.234$ on pig skin). However, if we compare the reduced relaxation functions of skin under compression with those of rat skin under tension [17], the compression curves are clearly distinguishable by their significantly smaller residual stress ratio G_∞ (Figure 3.14). Another key difference compared with that prior work is our use of skin from the hindimb, instead of dorsal skin, which is more commonly measured. The measurement of hindlimb skin is vital for studies of the sense of touch [6], known to be dependent on skin mechanical properties [36]. In particular, slowly adaptive type I (SAI) mechanosensitive afferents, essential for our ability to discriminate edges and curvature [3], display firing rate decay under constant displacement stimuli. This phenomena is known as adaptation and is dependent, in part, on the skin's viscoelastic relaxation [52]. We chose a hold phase at the maximum load position of 5 seconds to align with such adaptation and the typical length of neurophysiological recordings from SAI afferents [6]. Therefore, one would need to be careful in extrapolating the conclusions of this work outside of the chosen time window.
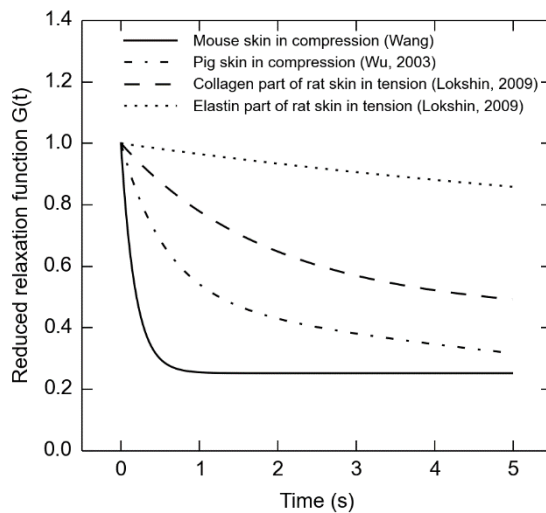
Figure 3.14 Comparison of the reduced relaxation function – Equation (3.3) – from measurement of different skin samples. Solid line is median data from work presented here on mouse hindlimb skin fitted to the one-term model, in the first experiment with median strain rate $\dot{\varepsilon} = 3.54\ s^{-1}$. Dotted-dash line is measurement from pig dorsal skin [22]. The dashed and dotted lines are both from rat skin, but the dashed line function is attributable only to collagen elements in the skin while the dotted function is only elastin elements [17]. Note that the skin in compression relaxes more than skin in tension.

Furthermore, the results of this work give important insights into issues currently being examined in the field of tactile mechanotransduction. SAI adaptation may carry information about a mechanical stimulus, for example, an object's compliance. Since thinner skin relaxes more than thicker skin, these data predict that the neural response from a population of SAI afferents in thin skin might adapt their firing rates to a greater extent than a similar population in thicker skin. This could negatively affect the ability of those with thin skin (e.g., the elderly population) to accurate assess tactile stimuli. In concordance with this, it is known that tactile acuity decreases with age [53]. Studies investigating changes in tactile sensation with aging or after injury usually focus on neuronal causes, but our results suggest skin mechanics might also contribute to changes in tactile

sensation. Our understanding of such mechanical properties – at the level of macro-scale compression – is important to develop realistic models of touch stimuli for haptic technology [36].

The results presented herein are based the assumption of a spatially homogeneous constitutive model; however, the skin is a heterogeneous and anisotropic material, and it is yet unclear what microscopic mechanisms underlie the nonlinear viscoelasticity we observe at the bulk level. Sub-micron studies have begun to suggest that individual skin layers indeed exhibit different degrees of viscoelasticity [20]. This may indicate that viscoelastic nonlinearity at the bulk level are dominated by one or more specific layers, such as the dermis, or a specific constituent, such as the interstitial fluid.

It is worth noting that there are some anatomical differences among various types of skin. The structure of skin differs between mouse hairy skin, our testing site, and glabrous skin. Hairy skin is composed of a thin epidermis that involutes deep into the dermis to form hair follicles. By contrast, glabrous skin, which lacks hair follicles, has a thick epidermis with undulating ridges at the dermal-epidermal junction. Human skin comprises the same fundamental layers as mouse skin with different thickness for each layer, with the exception that the muscular layer of panniculus carnosus in mouse skin does not exist in most areas of human skin [54]. In both species and both types of skin, the density and structure of the layers changes over the course of an animal's life, as the dermal papillary ridges flatten with age [55] and hair follicles undergo growth cycles [56]. While we have standard testing data for murine skin [15,17], the existing literature on human specimens covers only in-vivo viscoelastic measurement with complex stress fields, for example, Krueger et al. [13] investigated how viscoelasticity changes with aging using a Cutometer.

Future work on human skin specimens are needed to provide hyper-viscoelastic constitutive parameters, and the contribution of each layer to the skin's viscoelastic nonlinearities and the changes in these properties with age is yet to discover for both species, in order to be used for numerical simulations to better aid clinical practice.

Our work suggests that normal features of the neuronal response could be mediated by skin mechanics. In particular, we hypothesize that SAI afferents may adapt their firing rates more quickly to strong stimuli than to weak stimuli, since the skin relaxes more under high-strain conditions. Such changes in neuronal firing could be one mechanism by which the nervous system gains information about stimulus properties. Furthermore, SAI afferents may adapt their firing rates more quickly to faster stimuli than to slower stimuli, since the skin relaxes more quickly under higher strain rates [52,57]. This said, one must also note that intrinsic neuronal properties play a role in the overall adaptation of the mechanosensitive response independent of the skin's response. These results suggest a need to carefully control stimulus magnitude and velocity in performing electrophysiology experiments with tactile stimuli [36].

3.5 Acknowledgements

4 Aim II: Modeling neural responses amidst skin remodeling

4.1 Introduction

When we touch a surface, a diverse group of cutaneous afferents in our skin respond with trains of action potentials. Each class of afferents exhibits distinct firing patterns [3]. Their firing patterns may be attributed to particular end organ morphology, distinct ion-channel complements, and skin microstructure, among other factors. Even within a class of afferents, differences in physiological properties are observed. For example, for the same displacement stimulus, firing rates between slowly adapting type I (SAI) afferents can vary by about 30% during the sustained hold of a stimulus [8,28,58–60]. Such trends are observed for afferents both within and between animals. One source of this variance is proposed to be the architecture of peripheral end organs, in particular the skewedness in the distribution of Merkel cell-neurite complexes to heminodes within an arbor [7].

Differences in the skin's mechanics have also proposed to contribute to variance in firing properties of tactile afferents [12,14]. In fact, over the course of the mouse hair cycle, the thickness and elasticity of skin change dramatically over just days. For example, the thickness of the skin on the hind limb of the mouse spans a range from $125 - 607$ μm [15] between the ages of 6 and 34 weeks. Within just two weeks (10 to 12 weeks) a 36% percent increase in thickness is observed. Similarly, changes in the skin's elasticity are observed over the hair cycle, where the hyperelastic exponent can vary from $6.7 - 17.8$ and residual stress ratio from $0.04 - 0.49$ [61]. After the age of about 16 weeks in the mouse, hair growth occurs a mosaic pattern, such that

adjacent spatial locations differ in thickness and elasticity at a given time point [62–64].

Given the significant changes observed in the skin's mechanics over normal remodeling, it would be reasonable to connect the variance observed in skin measurements to variance observed in neuronal firing. Indeed, the skin's means of mechanical transformation – to convey stimulus information from its surface toward its interior layers where the tactile end organs reside – are a function of its thickness, elasticity, and time-dependent characteristics. Furthermore, prior work has shown that for stimuli with different widths of gratings and gaps, the trains of action potentials elicited from afferents are related, by the skin, to stimulus properties directly [28]. However, it is unclear whether naturalistic changes in skin mechanics can impact the neuronal response. In part, this is a difficult question to answer experimentally, though recent efforts have begun to directly manipulate the skin [65].

Herein we employ a computational modeling effort to ask whether the skin, given its changing properties, can reliably convey stimulus magnitude, rate and spatial geometry to the locations of tactile receptors. To answer this question, we employed finite element (FE) analysis of the skin, and varied the a) mechanical properties of mouse skin specimens, b) mode of stimulus control, and c) interior stress and strain quantities sampled near the locations of end organs. The local stresses and strains, which are interior pressure and deformation measures used in the field solid mechanics tied to surface forces and displacements, were the input to a leaky integrate-and-fire neuronal model. Under these computational conditions, we examined the impact of a naturalistic range of the skin's mechanics on the predicted neuronal response of SAI afferents.

4.2   Material and methods

4.2.1   Overall approach

We conducted three sets of exploratory computational experiments, building one upon another.

First, we sought to determine if measured differences in the skin's mechanics would affect

reaction forces at the stimulus tip, and by how much they would vary reaction forces. Using skin

thickness and elasticity values for six representative specimens (selected as described below) in

the mouse from a population of forty-one [15,61], we constructed six FE models (see Section 4.2.4)

to simulate the specimens amidst an ex vivo electrophysiological recording set-up [8] and

calculated reaction forces at the tip given its controlled displacement. Second, given that tip

reaction forces from the first experiment varied to a large degree, we sought to determine if

stresses and strains interior to the skin might vary similarly, and to what extent they might

influence firing rates. Therefore, we added to our model the spike firing response of an SAI

afferent based on a leaky integrate-and-fire algorithm (LIF) [7] and examined the resultant static

firing rates. Input to the LIF model were different measures of interior deformation, i.e.,

compressive strain, SED, and compressive stress, simulated under both controlled tip

displacement and tip force. Third, based on the observation from the second experiment that

small variance in neural responses were only predicted with the force-to-stress case, we sought

to more deeply understand why this particular case, is insensitive to changes in the skin's

mechanics, whereas the other measures are so sensitive. In so doing, we changed the simulation

paradigm. We began to use stimulus inputs that define the combined stimulus tip and skin surface

interaction rather than simply considering reaction forces at the rigid tip, since controlling a

stimulus by force does not account for probe geometry. For example, an equal magnitude of force

delivered to a small probe will concentrate over a smaller area of skin compared to a large probe.

Therefore, rather than tip displacements and forces, related stimulus input measures of

distributed deflection and pressure on the skin surface were used (Figure 4.1A). In addition, we sought to simulate three features of the neurophysiological response, i.e., stimulus magnitude, rate and spatial detail, instead of only considering interior deformation at the steady-state hold of the stimulus. Therefore, the metrics were expanded so as to analyze interior deformation over time, in terms of both i) magnitude during the entire ramp-and-hold of the stimulus and ii) rate of change over the stimulus ramp (Figure 4.1B). As well, we considered the iii) steady-state magnitude in the response of a population of afferents (Figure 4.1C).
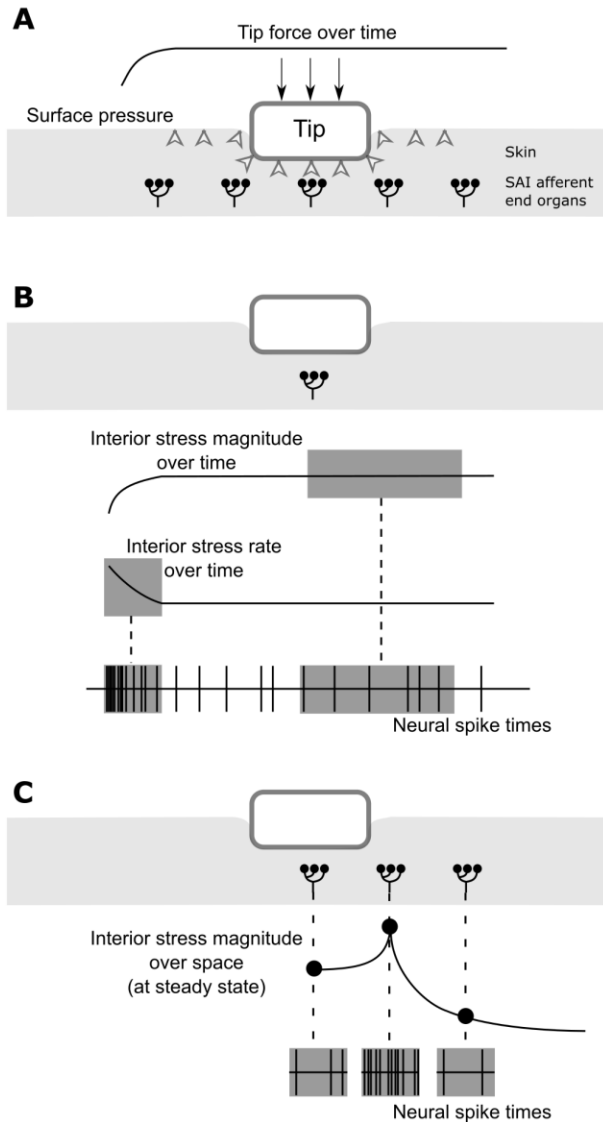
Figure 4.1 Schematic demonstrating the computational stimulation paradigm to represent three features of the neurophysiological response: stimulus magnitude, rate and spatial detail. A pressure-to-stress transformation is depicted in this example. A: When a ramp-and-hold force is applied at the rigid tip of 0.5 mm radius, it generates a distributed pressure on the skin surface, and thus creating interior stresses near the end organs of SAI afferents. The interaction of the stimulus in the skin is defined in terms of distributed pressure, as opposed to reaction force at the rigid tip. B: Considering just the center end organ of the five shown, the spike timings predicted during the static hold of the stimulus tie to the magnitude of interior stress, while the spikes predicted during the dynamic ramp tie to the rate of interior stress. C: Considering three end organs enclosed in boxes, the end organ beneath the indenter's edge would respond at a higher frequency because of a greater magnitude of interior stress at that location as compared to locations not directly beneath the edge or beneath the indenter.

Specifically, we utilized the techniques detailed below in this study.

4.2.2   Electrophysiological recording

<u>Skin-nerve preparation.</u> Used to fit and validate the numerical model, mouse *ex vivo* skin-nerve recordings were obtained essentially as described [6,8]. All animal use was conducted according to the National Institutes of Health *Guide for the Care and Use of Laboratory Animals* and was approved by the Institutional Animal Care and Use Committee of Columbia University (protocol AC-AAAC1561). An adult female transgenic mouse (*Atoh1/nGFP;* 8.3 weeks; 20 g) was used to record SAI responses on the proximal hind limb. Ramp-and-hold displacement stimuli were delivered to skin, with a nylon perfusion wick and Sylgard used as substrates. Sylgard is a silicone elastomer to mimic muscle tissue, and nylon serves to improve synthetic interstitial fluid circulation [6,8,44,66]. The minimum displacement used was 0.4 mm, which corresponds to 1.26 mN force and was the minimum stimulus required to consistently evoke a response. Ramp durations varied between $350 - 450$ ms, and the duration of the sustained load was 5 s.

<u>Calculation of dynamic ramp and static sustained hold firing rates.</u> Stimulus to skin contact was determined such that no action potentials (spikes) were elicited before contact, which we defined as 300 µm above the tip location at a force threshold of 0.25 mN. This was an empirical definition based both on the timing of the first spike and on forces being about three standard deviations above the noise. Given this contact position, two distinct phases of the stimulus were then identified [67]: a) dynamic ramp phase, defined from $t = 0$ s (i.e., stimulus to skin contact) to the time when peak force was achieved; b) static hold phase, defined from $t = 2$ to 4.5 s after peak force was achieved.

4.2.3 Computational modeling

The numerical models consist of FE and neural transduction sub-models.

Construction of the FE sub-model. The commercial software ABAQUS (Dassault Systèmes, Vélizy-Villacoublay, France) was used for FE analysis. An axisymmetric FE model (Figure 4.2) with hyper- and visco-elastic material properties was developed to mimic the reactions of the skin properties given indentation techniques of ramp-and-hold stimuli in both displacement and force control. The model comprised about 14,300 elements (element type CAX4RH, number of elements varies with change in skin thickness) and three layers to match those of the electrophysiological setup: skin, nylon perfusion wick, and silicone elastomer. Thickness and mechanical properties of the skin were set according to measurements by uniaxial compression [15,61], performed at a strain rate of 1.47 s^{-1} and fitted with a quasi-linear viscoelastic (QLV) model using a two-term Prony series with 1st-order Ogden hyperelasticity. In particular, of the seven required parameters, the four viscoelastic parameters $(g_1, g_2, \tau_1, \tau_2)$ and the first two hyperelastic parameters (μ_1, α_1) each takes the median value listed in Table 1 of the prior work [61]. The last hyperelastic parameter, D_1, uses the value $\frac{1}{10\mu}$, specifically chosen to follow the assumption that the skin is nearly incompressible, from previous measurement of the skin in compression [22] and other soft biological tissues [42], with an initial bulk modulus 20 times that of the initial shear modulus, corresponding to a Poisson's ratio ν of 0.475. Ogden hyperelasticity implies isotropy, whereas the skin is known to be anisotropic [1]. Similar to several prior works, the anisotropic nature of the skin is not considered herein. The isotropic model parameters fitted to uniaxial compression test data yield a good numerical representation for the case of indentation herein, where vertical

stress dominates. The skin thickness l_0 was set to 225 µm as is typical for a mouse hind-limb skin

thickness in telegon hair cycle [15]. Properties of nylon and Sylgard were obtained from inverse

FE model fitting with indentations by a spherical tip of 4 mm diameter. The 339 µm thick nylon is

fitted as a 1st-order Ogden hyperelastic material [68], with μ_1 and α_1 equal to 42.37 kPa and 9.0.

The 10.13 mm thick Sylgard substrate is fitted as a Neo-Hookean hyperelastic material [68] with

C_{10} as 105.2 kPa. Above the skin and substrate is a rigid body cylindrical indenter tip (0.5 mm

radius and with 0.1 mm radius edge-rounded fillet, based on that of the electrophysiological

setup). The surface interaction between indenter and skin was set as 0.3 [50,69]. At each time

increment of the simulation, seven types of quantities were extracted from model output, namely

the vertical force and displacement on rigid tip, distributed vertical deflection and contact

pressure at interaction surface, maximum compressive stress (σ_c), maximum compressive strain

(ε_c) and SED (w), which are all suggested by Sripati et al. [27]. We focused on these quantities

sampled in elements where the Merkel cell-neurite complexes (MCNC) are located, which is

defined for elements whose centroids are 22.5 µm beneath skin epidermal surface and will be

referred to as MCNC elements. The maximum compressive stress and maximum compressive

strain were calculated as

$$\sigma_c = -min\{\sigma_i\}, \varepsilon_c = -ln(min\{\lambda_i\}) \quad\quad\quad (4.1)$$

where σ_i, λ_i are the principal stresses and stretches.
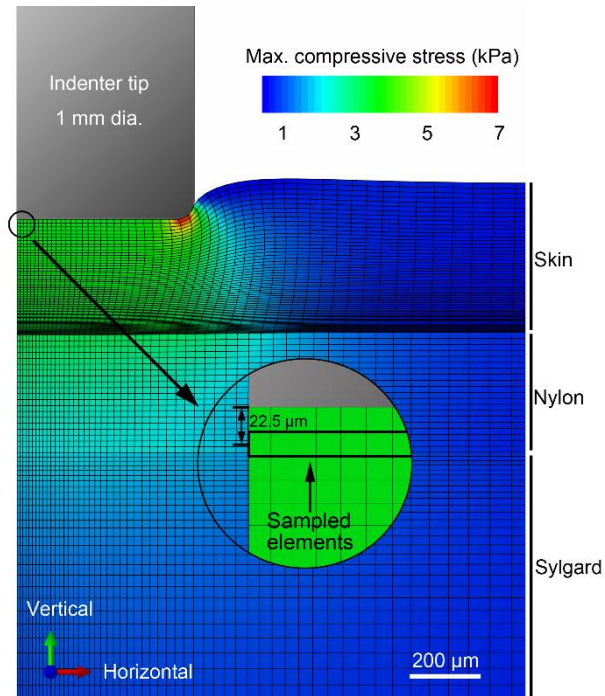
Figure 4.2 Illustration of the FE model used in the analysis. The axisymmetric model is constituted of three layers: skin, nylon and Sylgard, with approximately 14,300 elements. Hyper- and visco-elastic mechanical properties are used for all layers. Elements representing Merkel cell-neurite complexes are selected at 22.5 μm beneath the epidermal surface.

FE sub-model fitting and validation. Average static force versus average static displacement from the FE model were fitted to electrophysiological recordings (Figure 4.3A), where model displacements were linearly mapped to the recorded values. Then, we compared the force versus time curve from model to those from the recordings and observed good agreement (Figure 4.3B).
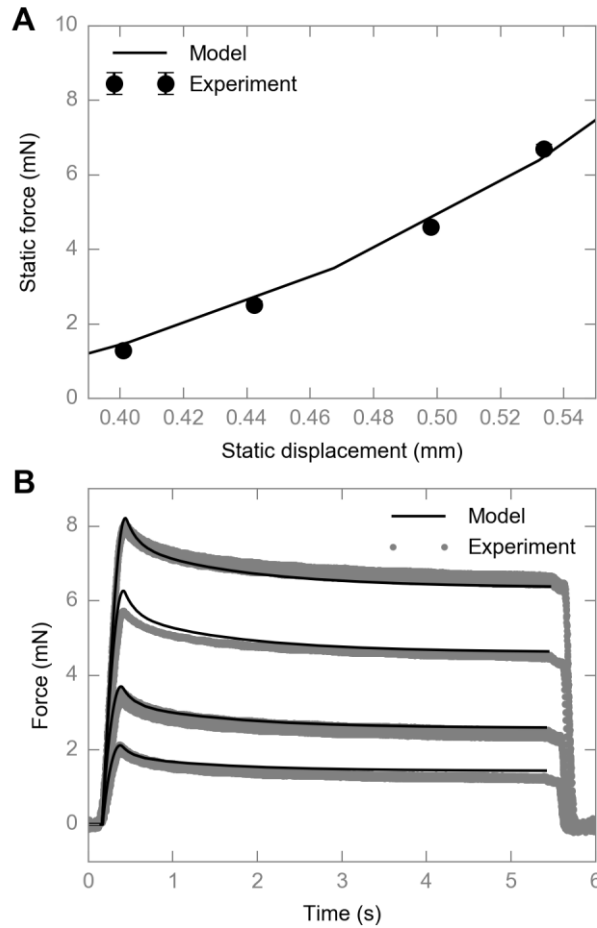
Figure 4.3 Comparison between the fitted FE model output and recorded force value during an electrophysiological experiment. A: Static force vs. static displacement, where the line represents the model output and the dots represent experiment measurements. Error bars are shown as standard deviations (not visible due to the low standard deviation values). B: Force traces vs. time. The solid line represents the model output, and the gray dots represent the aggregated experiment measurements. The animal used in this figure is a female GFP transgenic mouse at 8.3 weeks old.

Neural transduction sub-model fitting and validation. A previously published neural dynamics model for an SAI afferent [7] was used, with two modifications. First, instead of using only one type of interior deformation (SED) to feed into the neural sub-model, maximum compressive stress and strain were also tested. Second, the Gaussian noise term was not included in this effort, since the impact from noise is minimal compared to mechanical factors in this work. For simplicity,

we will refer to models with different mechanical output as stress-, strain- and SED-based models.

They share the same form of transduction current:

$$I_i(t) = M_i(k_0 q + k_1|\dot{q}|) + I_0 \text{ where } q = \sigma_c, \varepsilon_c \text{ or } w \tag{4.2}$$

In Equation (4.2), transduction current as a function of time for the i-th Merkel cell cluster was denoted as $I_i(t)$, two transduction coefficients as k_0 and k_1, number of Merkel cells on a heminode branch of the end organ as M_i, current intercept as I_0, and interior deformation and its temporal rate as q and $\dot{q}$, which may take any of the three quantities among maximum compressive stress σ_c, maximum compressive strain ε_c, or SED w. We used these three quantities to examine the three transformations of mechanical cues from skin surface to its interior, namely 1) deflection-to-strain, because they are both intrinsically geometric changes and the transformation is well-known [9]; 2) deflection-to-SED, for the wide usage of the SED quantity [7,11]; 3) pressure-to-stress, as stress has also been commonly used [27] and that both quantities are intrinsically force related. A typical grouping, where there are [8, 5, 3, 1] Merkel cells in each of four heminodes, is used in line with our prior study [7].

Each transduction current was then fed into a leaky-integrate and fire (LIF) model [7],

$$C\frac{dU_i}{dt} + \frac{U_i}{R} = I_i \tag{4.3}$$

where U_i are the voltage at each heminode, which will generate a spike when $U_i > U_{th}$ and reset all the heminodes in the MCNC. For simplicity, all voltages were shifted such that the resting potential is 0 mV. U_{th}, C, R are model constants taking values of 30 mV, 10 pF and 1.5 GΩ [7]. Most parts of the neural transduction sub-model was implemented in Python except for the LIF

model, which is implemented in C for performance and wrapped with the ctypes library to interface with Python.

Three neural sub-models were individually fitted to three stimulus trials from electrophysiological recordings. The model firing rate was calculated within span of dynamic and static phases individually in the same way done for the recordings. Then, we maximize the averaged coefficient of determination, denoted as R^2, between dynamic ramp and static hold phase. In each phase, the R^2 is calculated as

$$R^2 = 1 - \frac{\sum_i \left(r^n_{model} - r^n_{biological} \right)^2}{\sum_i \left(r^n_{biolgocial} - \overline{r_{biological}} \right)^2} \qquad (\,4.4\,)$$

The maximization was performed using the Sequential Quadratic Programming method [70]. The fitted transduction parameters of the representative fiber are listed in Table 4.1 and will be used in the following simulation. The R^2 goodness of fit is 0.86 for stress-based model, 0.86 for strain-based model and 0.76 for SED based model (Figure 4.4).

Table 4.1 Transduction parameters from fitting to SAI fiber. Note that all values are SI units.

Model	k_0	k_1	I_0
Stress-based	1.40E-16	1.68E-16	4.94E-12
Strain-based	2.73E-12	5.29E-12	4.66E-12
SED-based	1.46E-15	6.81E-15	7.59E-12
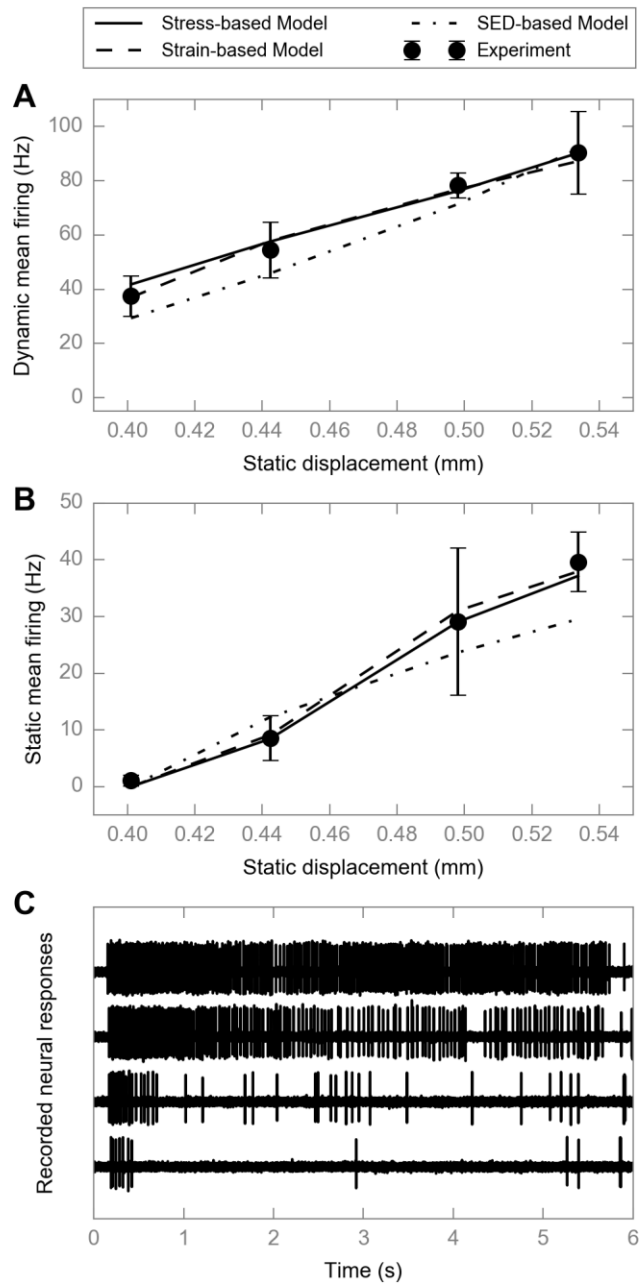
Figure 4.4 Results of fitting the neural sub-model to an SAI afferent response. A: model prediction vs. experiment recording for dynamic mean firing rate. Predictions from stress-based model are denoted with solid line, those from strain-based model are denoted with dashed lines, and those from SED-based model are with dotted-dash lines. Experiment recordings are solid dots with error bars denoting the standard deviation. B: similar with A, for static firing rate. C: representative neural responses at four displacements. The animal used in this figure is a female GFP transgenic mouse at 8.3 weeks old. For this recording, there were a total of thirteen stimulations, and two to four stimulus presentations per displacement.

Set-up for exploratory simulations. Computational simulations were run under both displacement and force control. We chose a span of stimulation magnitudes, experimentally observed to range from sub-threshold to fiber saturation. Specifically, for a 1.0 mm tip, displacements ranged between 0.34 to 0.73 mm and forces between 0 to 7.8 mN. To fill the range, we used five more stimuli, equally spaced in between those two at the limit. In sum, the seven stimuli are 0.34, 0.40, 0.47, 0.53, 0.60, 0.66, 0.73 mm for displacements and 0.00, 1.30, 2.60, 3.90, 5.20, 6.50, 7.80 mN for forces. By so doing, control of the surface deflection and pressure was achieved by clamping indentation displacement and force, in order to compare directly against electrophysiological recording data, as surface deflection and pressure are related to the skin surface and therefore slightly different from indentation displacement and force at a probe. As a consequence, the pressure traces are constrained within a certain range, rather than perfectly identical to each other. In all model simulations, parameters of the neural transduction function were held constant at the values obtained from fitting the neural transduction sub-model, and therefore the fluctuations in the internal deformation where SAI afferent end-organs reside, which are propagated from the surface stimulus, contributes all of the variance we observe in neural responses.

4.2.4   Representative sampling

To explore how changes in skin mechanics might impact neural firing rate, we performed computational simulations on a set of skin mechanical properties that span a representative cohort. Utilizing skin mechanics measurements from a past study [61] where each skin specimen was analyzed with seven independent parameters (four viscoelastic parameters of $\tau_1, g_1, \tau_2, g_2,$

two hyperelastic parameters of μ, α and skin thickness l_0), we describe the distribution of skin mechanics of the cohort ($N = 41$, all 7-9 weeks female mice) with a 41×7 population data matrix. Our objective was to find a $n \times 7$ sample data matrix for n representative samples, such that the corresponding sample covariance matrix maximizes its resemblance to the population covariance matrix. We quantify this likelihood with R^2 value, which represents the percentage of the population covariance being accounted for, calculated as

$$R^2 = 1 - \frac{\sum_{ij}\left(Cov_{sample}(X_i, X_j) - Cov_{population}(X_i, X_j)\right)^2}{\sum_{ij}\left(Cov_{population}(X_i, X_j) - \overline{Cov_{population}(X_i, X_j)}\right)^2} \qquad (4.5)$$

where X_i, X_j could be any two of the skin mechanics parameters with $i, j = 1, 2, \dots, 7$.

We used a greedy sampling algorithm to recursively draw samples from the population. For example, if we already have 3 specimens in the sample set, and 38 specimens left in the population, we pick one specimen from the 38 such that we have an updated sample set with 4 specimens. We calculate the covariance matrix of these 4 specimens and its resemblance value (R^2) to the population. We tried this for all 38 specimens left in the population and got 38 resemblance values. Among these, we found which sample yielded the best resemblance, for example Specimen #35, so we added this to the sample set. We then repeated the above process for the 37 specimens left in the population until we selected a sample set with a satisfactory R^2 value.

Formally, we used the following greedy algorithm for representative sampling:

1. Standardize the population matrix to standard normal distribution;

2. Find the average skin mechanics, defined as the specimen with least Euclidean distance to the population mean, and add it to the sample set;
3. Draw one specimen at a time among the rest of the population, and calculate the new sample covariance matrix if this sample was added to the existing sample set;
4. Identify the skin associated with the new sample covariance matrix that yields the largest population covariance matrix, and add it to the sample set;
5. Repeat steps 3-4 until enough of the proportion of the covariance matrix was accounted for.

The result of the above algorithm indicates that 82% of the population covariance can be accounted for at $n = 6$, and 90% at $n = 12$ (Figure 4.5). We chose to use $n = 6$ in this study to be sufficiently representative and computationally efficient at the same time. The specific skin mechanical parameters are listed in Table 4.2. Note that the average skin mechanics are labeled as Specimen #1.
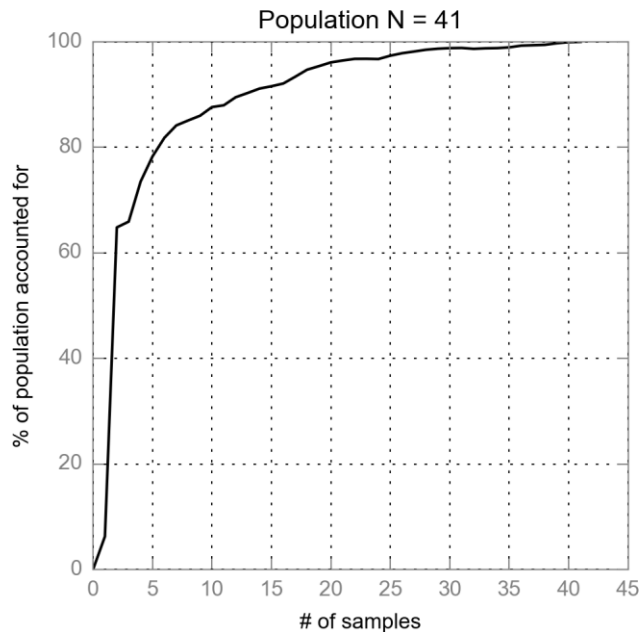
Figure 4.5 Relation between number of skin specimens and how well they represent the whole dataset. At n=6, 82% of the population covariance matrix is represented; at n=12, 90% of the population covariance matrix is represented.

Table 4.2 Mechanical properties of the 6 specimens used in the simulation. Variable names and units are in the parenthesis, where the no unit indicates that the values are dimensionless.

Skin #	Thickness (µm)	μ (Pa)	α	τ_1 (sec)	τ_2 (sec)	G_1	G_2	G_∞
1	379.81	1306.06	7.90	0.08	1.21	0.59	0.10	0.31
2	267.71	1153.32	9.37	0.03	0.41	0.73	0.15	0.12
3	388.58	1510.12	7.35	0.13	2.30	0.64	0.08	0.28
4	524.84	1653.94	9.25	0.18	2.07	0.47	0.10	0.43
5	435.53	1916.31	7.38	0.09	1.31	0.37	0.07	0.56
6	384.11	1554.02	9.35	0.03	0.31	0.52	0.21	0.27

4.2.5   Quantification metrics

We established quantitative metrics to augment the qualitative trends that could be observed in the results figures.

4.2.5.1   Comparing firing rates at the steady-state hold of the stimulus

We sought to determine the range of variance in predicted firing rates at each stimulus level given the range of skin mechanics of the six specimens. That is, for a displacement of 0.60 mm, how much would the predicted firing rates vary across the six skin specimens? Therefore, in the case of the 0.60 mm displacement, we subtracted 18 Hz as generated for skin specimen #3 (minimum firing rate) from 25 Hz as generated for skin specimen #2 (maximum firing rate). We calculated such differences in minimum and maximum firing rates for each of the five levels of displacement (0.47, 0.53, 0.60, 0.66, and 0.73 mm) and five levels of force (2.6, 3.9, 5.2, 6.5, and 7.8 mN). The average of those five predicted ranges, for example in the case of the displacement stimulus, are referred to as the absolute mean response range (MRR), in unit of Hz. We created MRR as a method of estimating variance because it is not typical for multiple specimens to be compared

and we sought to do so in a quantitative fashion. We also calculated a relative MRR by dividing the absolute MRR by the predicted firing rate at the middle of the displacement levels, i.e., 0.66 mm (or 6.5 mN for force), for the skin specimen (#1), which represents the average skin mechanics over the range of the six specimens. If one would assume a simple rate code, something unresolved and often discussed at the present, then the larger the MRR value, the less consistent would be the neural encoding of the stimulus magnitude, given differing skin mechanics.

4.2.5.2 Comparing transformations of surface stimulus to interior deformation

First, we characterized the robustness in the conveyance of surface stimulus magnitude from skin surface to its interior by examining the ranges of interior deformation across different skin mechanics under the same surface stimulus. To compare across different metrics of interior deformation, we examine whether the range of interior deformation caused by different specimens is large enough such that cues generated by different stimulus levels overlap. To quantify this, we developed the metric of skin-stimulus effect ratio (SSER). This measure describes variance in average interior magnitude of stresses and strains introduced by variable skin mechanics. To obtain SSER, we calculate the effect of skin by

$$Effect_{skin} = (max\ q_4 - min\ q_4) \text{ where } q = \sigma_c, \varepsilon_c \text{ or } w \qquad (\,4.6\,)$$

where q_4 denotes the average static interior deformation over $2-4.5$ seconds after the peak force was achieved of the 4th stimulus, and the max/min values are taken among all six representative specimens. Then we calculate the effect of stimulus by

$$Effect_{stimulus} = \frac{q_5 - q_3}{2} \text{ where } q = \sigma_c, \varepsilon_c \text{ or } w \qquad (\,4.7\,)$$

which denotes the average change in interior quantity when the stimulus changed from the 4th stimulus to the 3rd or the 5th. We obtain the SSER as

$$SSER = \frac{Effect_{skin}}{Effect_{stimuli}} \qquad\qquad (4.8)$$

The higher the SSER is, the more sensitive a mechanical transformation is to skin changes, and therefore the less robust does it convey the stimulus magnitude from skin surface to its interior.

Second, we characterized how well a mechanical transformation preserves stimulus rate and geometric features from surface stimulus to interior deformation by comparing the shape of the interior deformation and the surface stimulus with respect to its rate and spatial distribution. Quantitatively, we used the coefficient of determination (R^2 value) in comparing interior and surface stimuli. This measure describes the resemblance of the rate and geometric features of the surface and interior deformation. To calculate the R^2 value, we performed linear regressions with the interior deformation rate and spatial distribution as the independent variable, and those of the surface stimulus as the dependent variable. The R^2 values of these regressions represented goodness of preservation of stimulus rate and geometry features from surface stimulus to interior deformation. An R^2 value close to 1 indicates that the response is a perfect linear mapping to the stimuli, whereas an R^2 value close to 0 indicates the response is uncorrelated with the stimuli feature. Hence, the higher R^2 is, the better a mechanical transformation preserves rate and geometric features.

4.3 Results

Based on the combined results, we find overall that amidst changes in the skin's mechanics, the transformation of surface stimulus pressure to interior compressive stress conveyed stimulus information most reliably among the strategies tested. Other measures, such as surface

deflection-to-compressive strain or surface deflection-to-strain energy density (SED) or variants

thereon, distorted the interior deformation of the skin such that two stimuli can produce

comparable responses due to variance in skin mechanics alone.

In the first experiment, which examined the variance of the tip reaction forces, we observed

significant differences in reaction forces at the tip (Figure 4.6) in delivering the set of

displacements to each of the six models. For example, in Figure 4.6, given a displacement stimulus

of 0.60 mm the reaction force could vary from 2.8 – 5.0 mN, spanning a range of 2.2 mN solely as

a function of the skin mechanics. This is large compared to the force level of 1.26 mN that

consistently elicited a neural response from this SAI afferent (see Section 4.2.2).
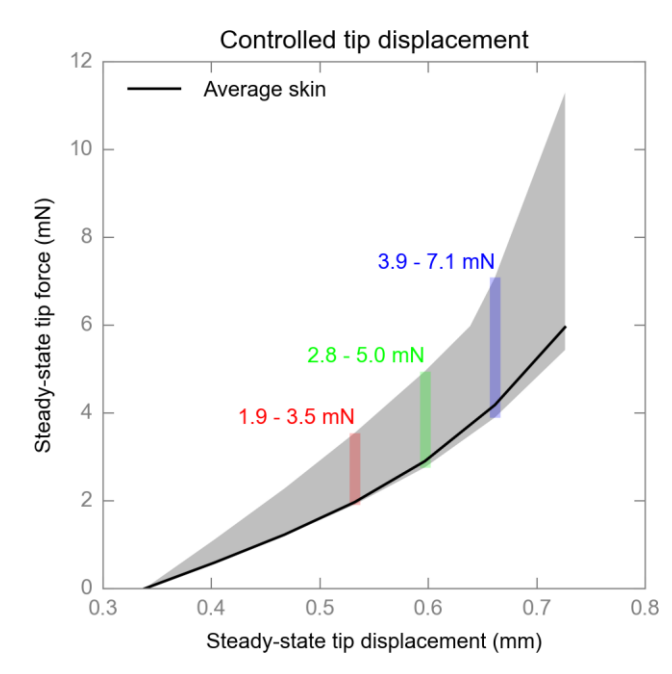
Figure 4.6 Under controlled displacement of the stimulus tip, skin mechanics can lead to substantial variations in reaction forces at the tip. Displacement and force values are plotted at steady-state, i.e., the 2-4.5 seconds after peak force was achieved. The solid black line denotes the force-displacement relationship given the skin properties of the average specimen, whereas

the grey shaded area denotes the range of its changes amidst the other representative skin samples. Red, green and blue bands each denote the reaction force yielding the quantities in Figure 4.8A, B, and C of the same colors.

The second experiment examined the variance of neural responses. Results indicated that static firing rates are indeed sensitive to changes in skin mechanics (Figure 4.7A-E), except when the stimulus is controlled by force and when compressive stress is used as input to the LIF model (Figure 4.7F). For example, in Figure 4.7A, given a displacement stimulus of 0.60 mm the firing rate could vary from 18 − 55 Hz, solely as a function of the skin mechanics. However, in Figure 4.7F, at a force stimulus of 7.80 mN the firing rate would vary much less, from 22 − 26 Hz. Quantitatively, we defined absolute and relative mean response range (MRR, for details see Section 4.2.5.1) to describe the variance, as shown in Table 4.3.
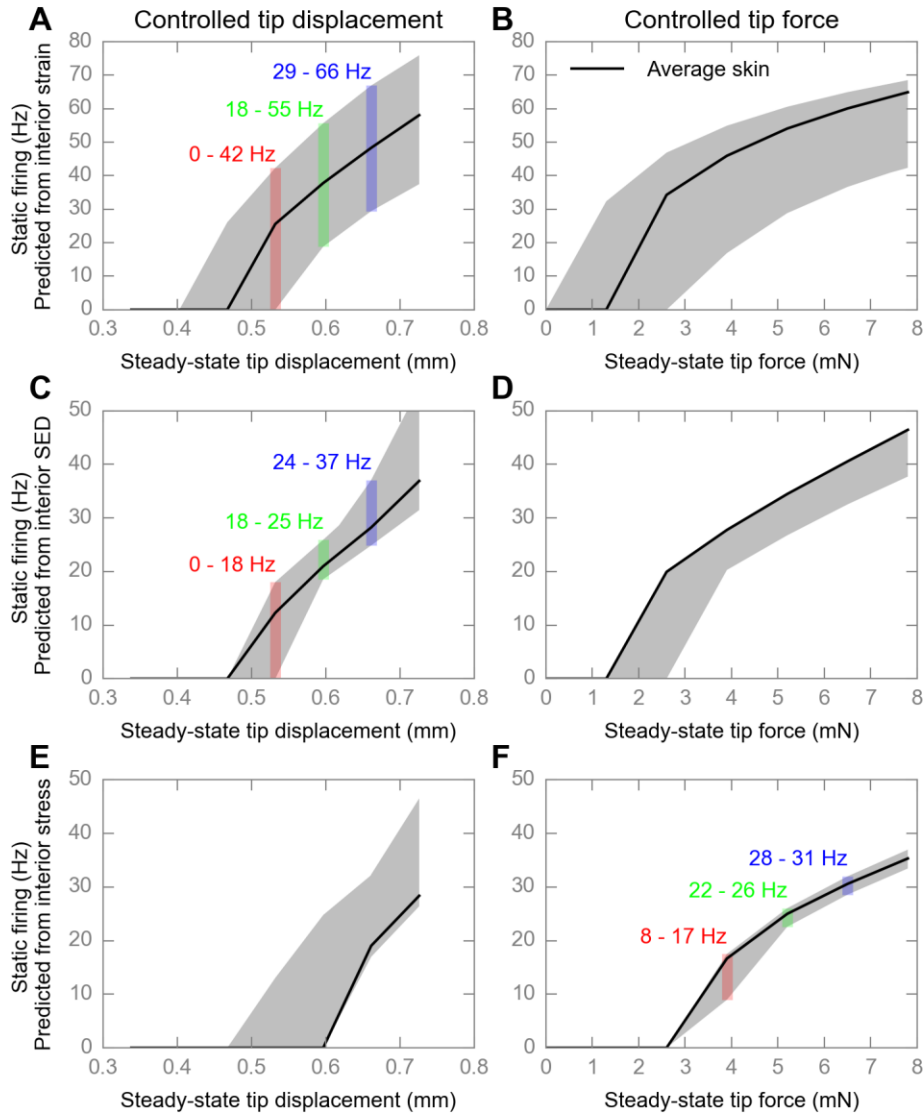
Figure 4.7 Simulated impact on how changes to skin mechanics influence predicted firing rates, as a function of the control of the stimulus (tip displacement or tip force) and interior deformation measure (interior strain, SED or stress). The two columns represent neural response as a function of tip displacement (panels A, C and E) or tip force (B, D and F), while the rows represent the prediction of strain- (A-B), SED-(C-D) and stress-based (E-F) models. Black solid lines denote the neural response given the skin mechanics of the average animal, and the grey shaded area denotes its range amidst the 6 representative skin samples. Red, green and blue bands in A, C and F each denote the predictions based on the quantities in Figure 4.8A, B, and C of the same colors.

71

Table 4.3 Quantification on how robustly the neural responses encode surface stimulus.

	Controlled displacement		Controlled force	
Predicted from	Absolute MRR (Hz)	Relative MRR	Absolute MRR (Hz)	Relative MRR
Strain	36.24	75%	34.22	57%
SED	12.11	43%	10.37	26%
Stress	14.66	77%	3.79	12%

The third experiment examined the three metrics in Figure 4.1A-C, and results are shown in Figure 4.8-4.10 respectively. In considering the stimulus over a ramp-and-hold time course of 5 s at three stimulus magnitudes (Figure 4.8), the results indicate that when skin mechanics change, the range of generated interior strain and interior SED are such that two stimulus magnitudes can overlap, and thereby be confused with each other. However, when the transformation of surface pressure to interior stress is used, the variance due to skin mechanics is minimal and the responses to the three stimuli are clearly separate. A quantification of inter-specimen response dispersion, which is a ratio between the inter-specimen and inter-stimulus effect (for details of the quantification refer to Section 4.2.5.2) is also shown in Table 4.4, where the pressure-to-stress transformation exhibited variance of an order of magnitude less compared to that of deflection-to-strain transformation.
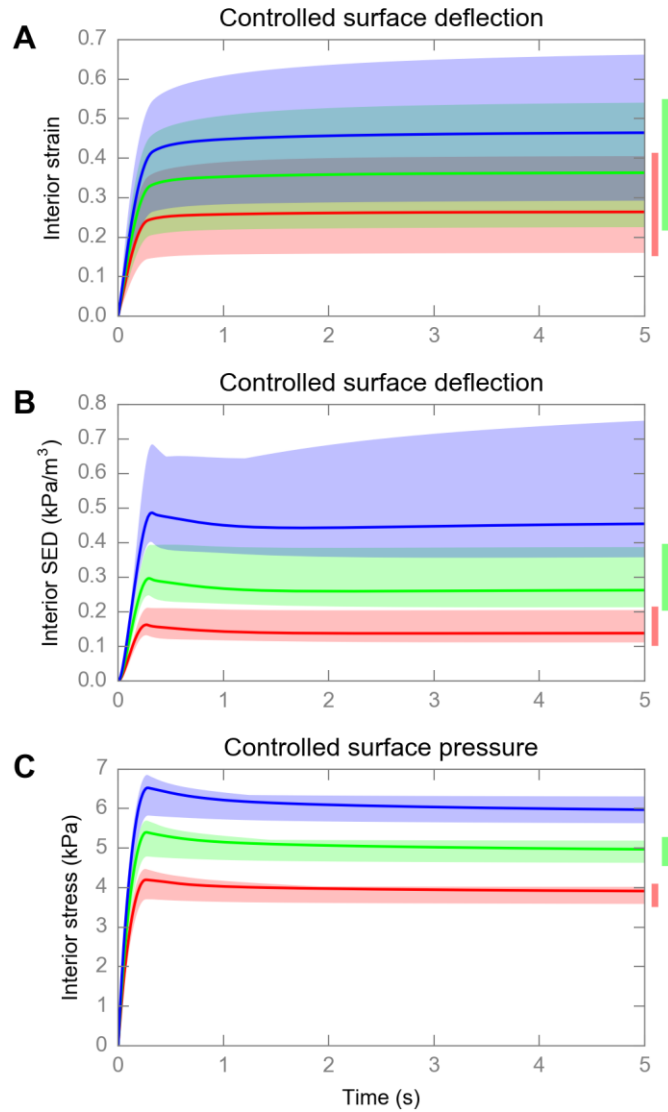
Figure 4.8 Computational experiment results showing variance in interior deformation when skin mechanics change. A: interior strain over time under controlled surface deflection; B: interior SED over time under controlled surface deflection; C: interior stress over time under controlled surface pressure. Red, green and blue area denotes the range of interior deformation under three different stimulation magnitudes, and solid lines denote the response of average skin mechanics. The bars to the right of the figures also redundantly show these ranges of interior deformation. Note that the predicted neural response at the steady-state of 2-4.5 seconds of red, green and blue strain traces in A is the same as those shown in Figure 4.7A.

Table 4.4 Quantitative evaluation of the three transformations from skin surface stimulus to its interior deformation. Skin-stimulus effect ratio (SSER) is used to understand how robust the

surface stimulus conveys the stimulus magnitude to interior deformation, and the R^2 of linear regression is used to understand how consistent the surface stimulus preserves the features of the stimulus rate and geometry to interior deformation.

	Variance in interior deformation ($SSER$)	Feature preservation (R^2)	
		Rate	Geometry
Deflection-to-strain	3.14	0.92	0.90
Deflection-to-SED	1.10	0.06	0.64
Pressure-to-stress	0.55	1.00	0.99

In considering the decelerating stimulus over a 0.25 second ramp into the skin surface, a similar trend was observed. That is, for the transformations of surface deflection to either interior strain or SED, the velocity profile at the skin surface and interior to the skin did not match one another (Figure 4.9A-B). However, under the transformation of surface pressure to interior stress rate the correspondence between the rate of change at surface and interior were quite well aligned (Figure 4.9C) with an R^2 value very close to 1 (Figure 4.9, Table 4.4) when linear regression is performed. Note that while many modeling efforts assume a constant velocity stimulus, our finger movements during tasks of active exploration usually decelerate in approaching a target [71]. This is similar to how most actuators operate as well. Accordingly, in our simulations, the tip accelerated in its movement in the air before contacting the skin and then gradually decelerated with a linearly decreasing velocity until being held at a depth or force into the skin.
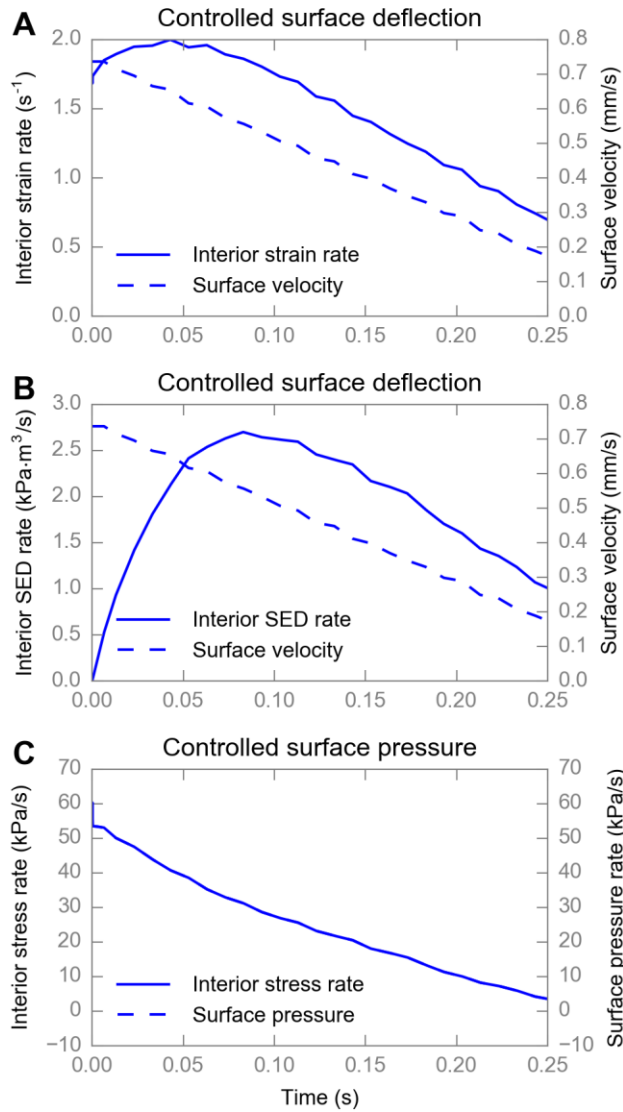
Figure 4.9 Computational experiment results showing the preservation of temporal features in interior deformation measures. During the first 0.25 seconds, the tip was gradually decelerating with a linearly decreasing velocity, and eventually stopped to hold its position at the skin surface. A: interior strain rate and surface velocity over time differ in shape; B: likewise interior SED rate and surface velocity over time differ in shape; C: interior stress rate and surface pressure rate are similar in shape, in fact overlapping each other. All traces are generated from simulations using the average skin.

In considering the stimulus at the steady-state period over $2 - 4.5$ s after peak force was achieved

but over a lateral volume that represents the positions of a population of afferents, a similar trend

was observed. That is, for only the case of the transformation of pressure-to-stress was the surface geometry of the 0.5 mm radius cylindrical tip faithfully represented in the interior stress (Figure 4.10), as its spatial distribution almost replicated that of the surface pressure ($R^2 = 0.99$, Table 4.4). For details of the quantification refer to Section 4.2.5.2.
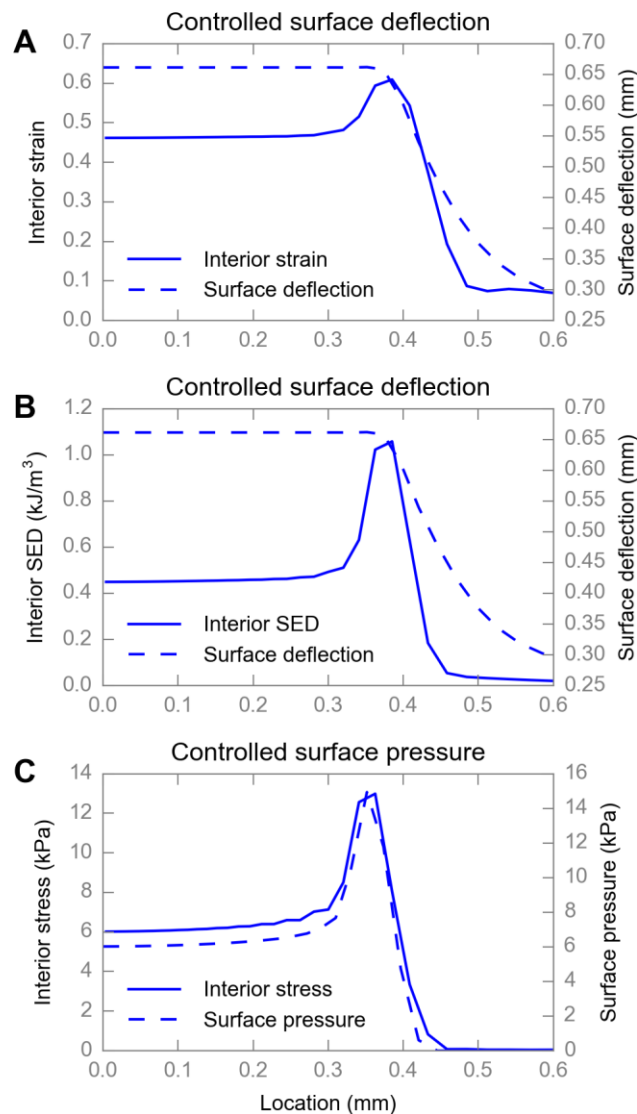
Figure 4.10 Computational experiment results showing the preservation of spatial surface geometry of the stimulus in interior deformation measures. Under the tip of 0.5 mm radius with 0.1 mm radius fillet, the stress-strain field at SAI afferent end organ location is uniform at the tip

center (0 mm location) and is most concentrated at the tip edge (around 0.5 mm location). A: interior strain and surface deflection over space differ in shape; B: interior SED and surface deflection over space differ in shape; C: interior stress and surface pressure over space are very similar in shape. All traces are generated from simulations using the average skin.

4.4 Discussion

Given that the skin's mechanics, i.e., thickness, elasticity and time-dependent characteristics, change over an animal's lifespan, we sought to investigate if such changes might cause variability in an afferent's firing properties. In this study, we took a computational approach to the problem, using finite element analysis as well as neural dynamics models fitted to an electrophysiological recording. The hyper- and visco-elastic constitutive models employed a range of skin measurements observed over the hair cycle in mice. The computational results suggest that even amidst such changes in the skin's mechanics, the skin can reliably convey indentation magnitude, rate and spatial geometry to the location of a tactile end organ of an SAI afferent, i.e., a Merkel cell-neurite complex. However, this is only the case when the stimulus tip is controlled by surface pressure and compressive stress is measured near the end organ's location. This robust transformation implies a way to help maintain consistent touch encoding during the dynamics of skin remodeling. Furthermore, from a behavioral perspective, stimulus control by these means may more closely tie to how we actively explore our environment.

This study employs an emerging research paradigm in which computational modeling is used to develop testable hypothesis [72]. Although the computational results are highly suggestive, experimental studies will be required to test the hypothesis definitively. For example, one might modify skin properties over a range of animals, perhaps by controlling subcutaneous fat independent of age. That said, there is some electrophysiological literature to support the results

herein. Recent neural recordings with a force-controlled stimulus confirm that mean firing rates of human SAI afferents do not vary with skin mechanics altered through venous occlusion [65]. This result agrees with our model prediction, although experiments with a displacement-controlled stimulus are still lacking to fully test our model's predictions. In addition, while this is consistent with our prediction, one might question whether the skin manipulation was naturalistic. Another recent study in C. elegans compared force and displacement indentation and considered tissue viscoelasticity [73]. However, rapidly adapting responses were the focus, and their responses were tied to displacements. With respect to slowly adapting responses, prior efforts have compared neural responses as a function of controlling stimulus force, displacement and nominal pressure. Firing rates in the early periods of the sustained hold were reported to correlate more with displacement [23], firing rates in the later periods of the sustained hold correlate more with force [74] and firing rates in early (< 2 s) and late (> 4 s) periods correlate more with nominal pressure [75]. The results of the latter effort are similar to those found herein, though that work did not consider a range of skin specimens.

Moving to the behavioral level, our finding that pressure at skin surface, rather than deflection, is a more robust environmental cue echoes theories that human subjects actively control force rather than displacement at the finger pad and other grasp surfaces during daily activities. Force directly converts to pressure on the skin, and such a conclusion fits our intuition, especially when visual cues are eliminated. For example, we prevent slips by controlling grip force while measuring the frictional condition through cutaneous mechanoreceptors [37]. We also adjust exploratory forces to optimize our perception of object compliance [76]. The underlying mechanism for the pressure-to-stress transformation is Newton's Third Law of Motion. This guarantees that whenever a pressure is applied from external environment, the skin will instantaneously respond

with an identical amount of pressure in the opposite direction, independent of skin mechanics. Hence, the stimulus must be truly reflected internally. On the other hand, when surface deflection is applied, corresponding changes in volume - strain, is not only dependent on the stimuli applied but also on the skin mechanics and is therefore variable. As for the interior deformation, pressure is intrinsically tied to compressive stress, since they are simply modes of different projections of the Cauchy stress tensor: pressure on the normal direction of contact, and maximum compressive stress the principal direction of minimum principal stress. During an indentation, normal force usually dominates so the normal direction would coincide with the principal direction of minimum principal stress. Therefore, maximum compressive stress will resemble the value of pressure very closely independent of the amount of strain. SED, on the other hand, depends on both stress and strain, the latter of which is dependent on skin mechanics.

We suggest that pressure is an optimal stimulus, instead of displacement or force. Indeed for the computational analysis of interior deformation in Figure 4.8 – 4 the results are framed in terms of surface pressure. However in indenting with a mechanical indenter in practice, one cannot so readily control surface pressure. One might think to control force and then divide by the area of the tip to get "nominal pressure" and indeed this surface quantity, which Ge and Khalsa referred to as compressive stress, better correlates with firing rate than displacement or force [75]. That said, this method does not account for complicated contact mechanics. These include both frictional slip and skin deformation at the edge of the tip. Preliminary computational estimates are that nominal pressure can be quite inaccurate. For example for a 1.0 mm diameter tip, a force of 4.1 mN generates a surface pressure of 4.06 kPa at the tip's center whereas the nominal pressure is 5.22 kPa (29% larger). The magnitude of such differences depend upon tip size. For a 1.5 mm diameter tip, the nominal pressure would only be 4.26 kPa (6% larger) than a surface

pressure of 4.03 kPa. Controlling stimulus pressure in practice will have to be coupled tightly with mechanical analysis that accounts for the intricacies of the contact mechanics.

Among the interior deformation quantities tied to afferent response, our work shows that maximum compressive stress is most robust to changes in the skin and best resembles the rate and spatial distribution contact pressure at the skin surface. Many interior deformation quantities have been considered previously [9–11,27,77–79]. However, maximum compressive stress is invariant to rotations, unlike others such as maximum horizontal or vertical stress, which were excluded from analysis following past studies [27]. Also, when compared against other commonly used measures such as Von Mises stress, the measure of maximum compressive stress can account for hydrostatic pressure. Moreover, we considered other principal stresses such as maximum tensile stress and maximum absolute principal stress, although these were not included here because a very minimal tensile stress field was present. The measure of maximum compressive stress has a clear physical meaning: the maximum pressure on the receptor in any direction [27].

Finally, one might ask which factors most influence the variability in the neuronal firing properties between afferents. A recent study from our group proposed that some of this variance can be accounted for by the architecture of tactile end organs, in particular the skewedness in the distribution of Merkel cell-neurite complexes to heminodes within an afferent's arbor [7]. Based on the present study, it is tempting to suggest that the skin plays little role relative to end organ morphology, distinct ion-channel complements, and other intrinsic neuronal factors; however,

we note that this is a different question. To consider the relative variance of these factors in the context of one another is an interesting future question.

4.5 Acknowledgements

5 Overall conclusions and future work

In this dissertation, we detailed two major efforts. First, we quantified how compressive viscoelastic properties of mouse skin distribute among population, and identified that they correlate with thickness, stretch level and rate. This is the first in the literature to comprehensively survey skin compressive viscoelasticity and revealed its correlations with skin thickness and loading conditions. Second, we computationally modeled how thickness-related viscoelasticity impact neural responses of tactile afferents, and identified that the use of surface stimulus of pressure and interior deformation of stress minimizes the variance introduced by skin mechanics changes. To the best of our knowledge, this is the first to show that the skin can reliably convey surface stimulus even amidst changes in skin mechanics, and identified the naturalistic stimulus of pressure for tactile receptors from a mechanistic point of view.

This work only exploited the thickness-dependent viscoelasticity of skin mechanics when exploring its implication on tactile responses in Aim I, and has not taken fully advantage of the richness in the data from Aim I. In fact, all three factors identified in Aim I that the skin viscoelasticity depend on may impact SAI afferent responses: a) when the same ramp-and-hold displacement stimulus is applied, different skins will cause different spiking patterns due to a change in thickness (Figure 5.1A); b) for the same skin, different displacements will cause different stretch levels and impact the neural responses (Figure 5.1B); c) or, displacement stimulus at different ramp velocity will introduce different stretch rates and therefore stress relaxations to generate different spike traces (Figure 5.1C). We decided to study a) and focus on the late-hold phase of the stimulus, which we already have a relatively well-controlled experiment dataset; in contrast, investigations into both b) and c) will depend on experimental data that involves confounding factors from variance in neural dynamics. For b), the neural responses might be suppressed when displacement increase in addition to the effect from stretch-dependent viscoelasticity. For c), the sensitivity to a moving stimulus and neural adaptation rate during the early-hold phase of the stimulus will all confound the observable effects from a change in rate-dependent viscoelasticity. Nevertheless, these two difficult questions are of great interest if we want to understand the basic phenomenon of neural adaption in mechanosensitive afferents and should be closely looked into in future work.
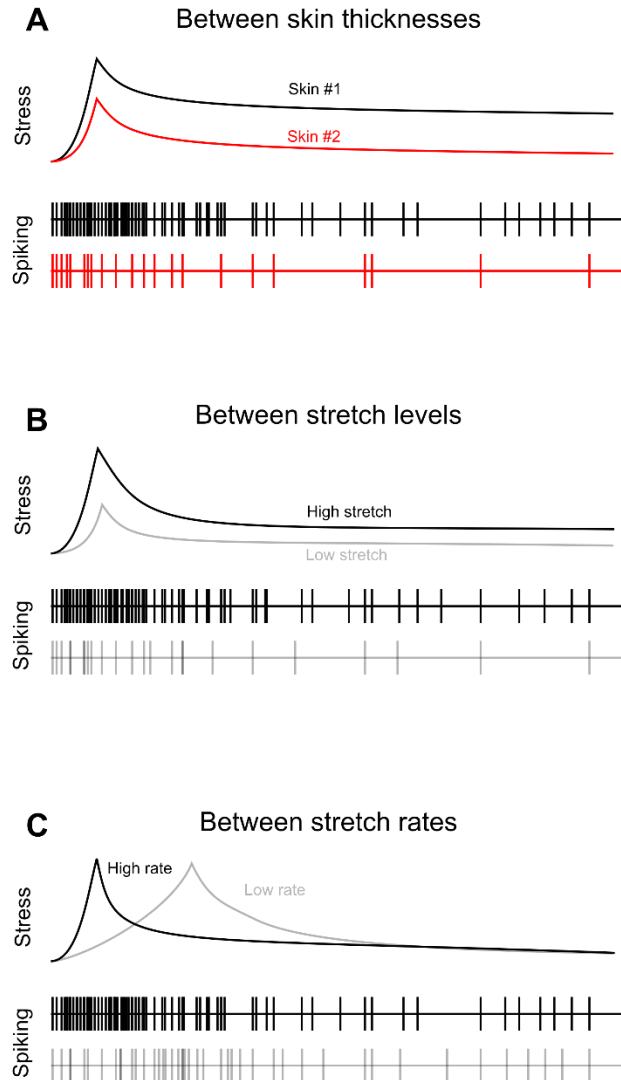
Figure 5.1 Impact of skin viscoelasticity on SAI afferent responses under ramp-and-hold displacement stimulus. A: For the same displacement applied, different skin thicknesses will yield different stress-time curves and therefore spiking patterns. B: For the same skin, stimulus at different displacements will introduce stress traces that relaxes differently due to change in stretch levels, and therefore impacts the neural responses. C: For the same skin, displacement stimulus at different ramp velocity will introduce different stretch rates and therefore stress relaxations, causing the spiking pattern to vary.

The Aim II modeled an ex-vivo electrophysiological setup on mouse hindlimb skin, in contrast to in-vivo experiments in primate or human fingertips. We have chosen this approach since it best serves our questions asked herein related to the variability in biological systems. In order to characterize the distribution of skin mechanics and neural responses among a population of samples, we need a) a large number of experiments to be performed, which requires a considerable amount of subjects; and b) in each experiment, the conditions need to be highly controlled and protected from external noises as much as possible. This is much easier to do in mouse compared to primates or human. First of all, mouse are much lower in cost for a large sample size used in this study; secondly, we can strictly control the strain and diet of mice which is virtually impossible for human subjects. In addition, the ex-vivo preparation provides a consistent boundary condition for the nerve recorded and eliminated the noise from differences in the mechanics of underlying muscles and bones. Those said, we will eventually be more interested in how those mechanisms apply to human, where we will rely on experiments with human subjects, as a potential direction for future work.

The Aim II heavily relied on computational study, which differs from the traditional experiment-based approach in mechanotransduction studies. While the hypothesis will be ultimately tested via experiments, computation can be used to identify hypotheses as preliminary explorations. In addition to the reduced cost and time, computations have the advantage to strictly control the conditions in experiments. For example, during an electrophysiological recording neither the neural dynamics nor skin mechanics will be identical between two animals, therefore we have to increase the sample size to achieve adequate statistical significance. In contrast, we can easily fix one factor to be identical between experiment runs and only vary the other in a numerical simulation. Lastly, computational studies provide us with mathematical insights that are not

directly observable in experiments, such as the changes in interior stress and stresses inside the skin. Nevertheless, the computational experiment will need to be validated via lab experiments in the future work.

For the first time, this work predicted from a mechanistic point of view that the SAI afferent end organs respond to interior stresses, rather than strain or strain energy densities. In contrast, prior study [27] made similar predictions based on empirical goodness of fitting to experiment data, and therefore may be sensitive to the specific experimental conditions. Nevertheless, all interior deformations discussed above are based on the continuum assumption of the skin along with arrays of cutaneous mechanoreceptors. Ultimately, these predictions will need to be modeled at a lower level that depicts the fine structures of the end organs, and validated through direct experiment observations, when we are no longer constrained by the existing technology that limits us to monitor the stress state inside the mechanoreceptors.

Future Directions. The underlying mechanism of SAI afferents' unique physiology still largely remains unknown. For example, what is the local mechanical stimulus that opens the mechanosensitive channels in SAI afferents? To answer this question, more detailed investigations in both biomechanics modeling and electrophysiological experiments are necessary. On the former, the skin no longer approximates to a continuum at the scale of a single Merkel cell, but exhibits its non-linear structural properties. Therefore, one must take how interstitial fluid interacts with the cell membrane and connective fibers into account to realistically model the activation process of mechanosensitive channels. On the latter, one need to refine the control in electrophysiological experiments by decoupling the role each skin constituents, such as collagen

and elastin fibers, interstitial fluid and the proteoglycan fillers, on the opening and closing of mechanosensitive channels.

Summary on the scope of the dissertation. The work during my PhD study with Dr. Gerling, I have mainly worked in two areas: a) measurement of skin mechanics under compression, and b) computational modeling of SAI afferent responses. The intersection between the two efforts constitutes this dissertation, as an attempt to understand if and how our tactile system may work amidst changes in skin mechanical properties to maintain the consistency of our touch perception (Figure 5.2). They are also published as individual journal papers in:

- Wang, Y., Marshall, K. L., Baba, Y., Lumpkin, E. A., and Gerling, G. J., 2015, "Compressive viscoelasticity of freshly excised mouse skin is dependent on specimen thickness, strain level and rate," PLoS One, **10**(3), p. e0120897.

- Wang, Y., Baba, Y., Lumpkin, E. A., and Gerling, G. J., "Computational modeling indicates that surface pressure can be reliably conveyed to tactile receptors even amidst changes in skin mechanics.," J. Neurophysiol., in press.

Summary of publications: 2 journal articles published; 1 journal article in press;
1 journal article under review; 1 journal article in preparation;
2 conference papers published.
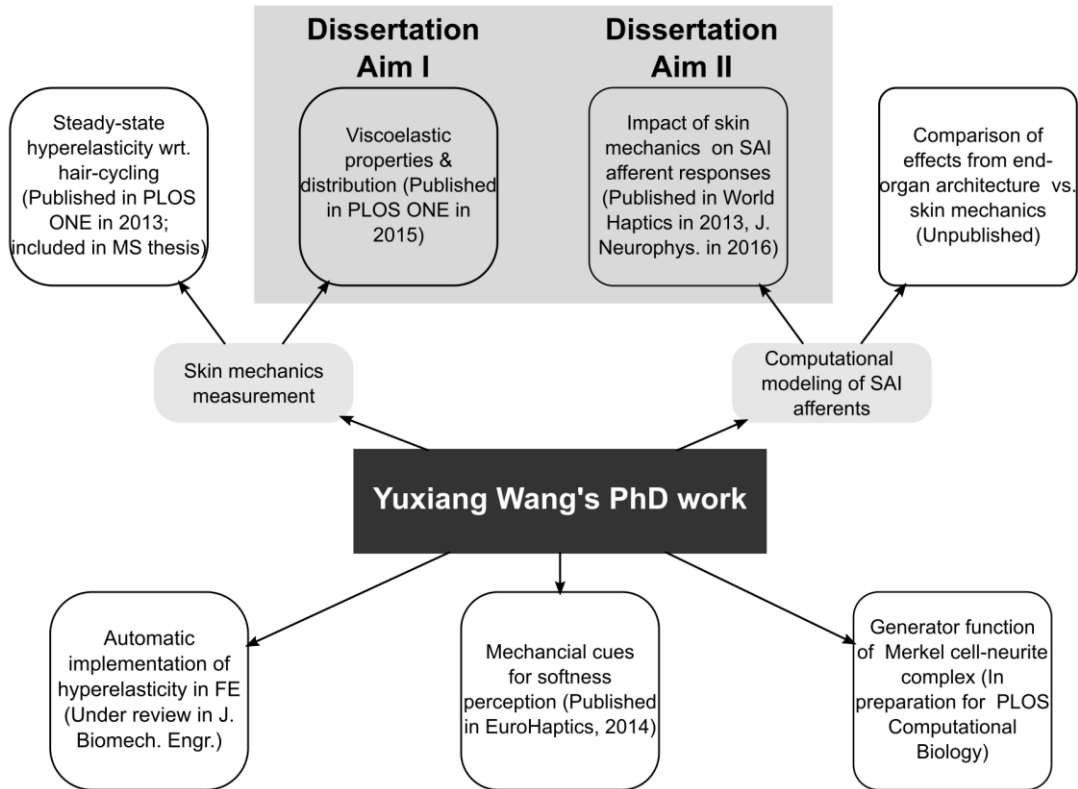
Figure 5.2 Scope of the dissertation amidst my work during PhD study with Dr. Gerling.

Other journal papers that are not included in this dissertation are:

- Wang, Y., Marshall, K. L., Baba, Y., Gerling, G. J., and Lumpkin, E. A., 2013, "Hyperelastic material properties of mouse skin under compression," PLoS One, **8**(6), p. e67439.

- Wang, Y., and Gerling, G. J., "Automatic numerical evaluation of stress and tangent modulus for hyperelastic material implementation in finite element analysis," under review in J. Biomech. Eng.

- Wan, L., Wang, Y., Baba, Y., Lumpkin, E. A., and Gerling, G. J., "A stimulus independent generator function of Merkel cell-neurite complex," in preparation for PLoS Comput. Biol.

- Lesniak, D. R., Wang, Y., Marshall, K. L., Lumpkin, E. A., and Gerling, G. J., "Computational modeling predicts that tactile end-organ plasticity offset changes in skin thickness during target-organ remodeling," manuscript on hold and waiting on more experiment results.

Published peer-reviewed conference papers during my PhD studies are:

- Wang, Y., and Gerling, G. J., 2014, "Computational modeling reinforces that proprioceptive cues may augment compliance discrimination when elasticity is decoupled from radius of curvature," **8619**, pp. 360–368.

- Wang, Y., Marshall, K. L., Baba, Y., Lumpkin, E. A., and Gerling, G. J., 2013, "Natural variation in skin thickness argues for mechanical stimulus control by force instead of displacement," 2013 World Haptics Conference, WHC 2013, IEEE, Daejeon, Korea, pp. 645–650.

Non-peer-reviewed conference abstracts are:

- Wang, Y., Baba, Y., Lumpkin, E. A., and Gerling, G. J., 2016, "Computational modeling indicates surface pressure can be reliably conveyed to tactile receptors even amidst changes in skin mechanics," IEEE Haptics Symposium, Philadelphia, USA.

- Wang, Y., 2015, "Automatic numerical evaluation of stress and tangent modulus for hyperelastic material implementation in finite element analysis," The 13th International Symposium, Computational Methods in Biomechanics and Biomedical Engineering, Montreal, Canada.

- Wang, Y., Marshall, K. L., Baba, Y., Lumpkin, E. A., and Gerling, G. J., 2013, "Viscoelasticity of mouse skin under compression is dependent on level of strain.," Proceedings of the 11th International Symposium, Computational Methods in Biomechanics and Biomedical

Engineering, Salt Lake City, USA, pp. 103–104.

- Marshall, K. L., Jenkins, B. A., Wang, Y., Lesniak, D. R., Gerling, G. J., and Lumpkin, E. A., 2014, "Elucidating mechanisms of touch receptor plasticity during target organ remodeling," Society for Neuroscience 44th Annual Meeting.

- Marshall, K. L., Baba, Y., Jenkins, B. A., Wang, Y., Lesniak, D. R., Gerling, G. J., and Lumpkin, E. A., "Elucidating mechanisms of touch-receptor plasticity during target-organ remodeling," Society of General Physiologists 68th Annual Meeting and Symposium.

References

[1]   Lanir, Y., and Fung, Y. C., 1974, "Two-dimensional mechanical properties of rabbit skin—II. Experimental results," J. Biomech., **7**(2), pp. 171–182.

[2]   Wang, Q., and Hayward, V., 2007, "In vivo biomechanics of the fingerpad skin under local tangential traction.," J. Biomech., **40**(4), pp. 851–60.

[3]   Johnson, K., 2001, "The roles and functions of cutaneous mechanoreceptors," Curr. Opin. Neurobiol., **11**(4), pp. 455–461.

[4]   Quindlen, J. C., Lai, V. K., and Barocas, V. H., 2015, "Multiscale Mechanical Model of the Pacinian Corpuscle Shows Depth and Anisotropy Contribute to the Receptor's Characteristic Response to Indentation.," PLoS Comput. Biol., **11**(9), p. e1004370.

[5]   Bautista, D. M., and Lumpkin, E. A., 2011, "Perspectives on: information and coding in mammalian sensory physiology: probing mammalian touch transduction.," J. Gen. Physiol., **138**(3), pp. 291–301.

[6]   Wellnitz, S. A., Lesniak, D. R., Gerling, G. J., and Lumpkin, E. A., 2010, "The regularity of sustained firing reveals two populations of slowly adapting touch receptors in mouse hairy skin.," J. Neurophysiol., **103**(6), pp. 3378–88.

[7]   Lesniak, D. R., Marshall, K. L., Wellnitz, S. A., Jenkins, B. A., Baba, Y., Rasband, M. N., Gerling, G. J., and Lumpkin, E. A., 2014, "Computation identifies structural features that govern neuronal firing properties in slowly adapting touch receptors," Elife, **3**, pp. e01488–e01488.

[8]   Maksimovic, S., Nakatani, M., Baba, Y., Nelson, A. M., Marshall, K. L., Wellnitz, S. A., Firozi, P., Woo, S.-H., Ranade, S., Patapoutian, A., and Lumpkin, E. A., 2014, "Epidermal Merkel cells are mechanosensory cells that tune mammalian touch receptors.," Nature, **advance**

on.

[9]   Phillips, J. R., and Johnson, K. O., 1981, "Tactile spatial resolution. III. A continuum mechanics model of skin predicting mechanoreceptor responses to bars, edges, and gratings.," J. Neurophysiol., **46**(6), pp. 1204–25.

[10]   Gerling, G. J., Rivest, I. I., Lesniak, D. R., Scanlon, J. R., and Lingtian Wan, 2014, "Validating a Population Model of Tactile Mechanotransduction of Slowly Adapting Type I Afferents at Levels of Skin Mechanics, Single-Unit Response and Psychophysics," IEEE Trans. Haptics, **7**(2), pp. 216–228.

[11]   Dandekar, K., Raju, B. I., and Srinivasan, M. A., 2003, "3-D finite-element models of human and monkey fingertips to investigate the mechanics of tactile sense.," J. Biomech. Eng., **125**(5), pp. 682–91.

[12]   Daly, C. H., and Odland, G. F., 1979, "Age-related changes in the mechanical properties of human skin.," J. Invest. Dermatol., **73**(1), pp. 84–7.

[13]   Krueger, N., Luebberding, S., Oltmer, M., Streker, M., and Kerscher, M., 2011, "Age-related changes in skin mechanical properties: a quantitative evaluation of 120 female subjects.," Ski. Res. Technol., **17**(2), pp. 141–8.

[14]   Escoffier, C., de Rigal, J., Rochefort, A., Vasselet, R., Leveque, J.-L., and Agache, P. G., 1989, "Age-related mechanical properties of human skin: An in vivo study.," J. Invest. Dermatol., **93**(3), pp. 353–357.

[15]   Wang, Y., Marshall, K. L., Baba, Y., Gerling, G. J., and Lumpkin, E. A., 2013, "Hyperelastic Material Properties of Mouse Skin under Compression," PLoS One, **8**(6), p. e67439.

[16]   Daly, C. H., 1982, "Biomechanical properties of dermis.," J. Invest. Dermatol., **79**(s1), p.

17s–20s.

[17]   Lokshin, O., and Lanir, Y., 2009, "Viscoelasticity and preconditioning of rat skin under uniaxial stretch: microstructural constitutive characterization.," J. Biomech. Eng., **131**(3), p. 031009.

[18]   Martin, P. G., 2000, "Properties of human skin," PhD dissertation, University of Virginia.

[19]   Lanir, Y., and Fung, Y. C., 1974, "Two-dimensional mechanical properties of rabbit skin—I. Experimental system," J. Biomech., **7**(1), pp. 29–34.

[20]   Crichton, M. L., Donose, B. C., Chen, X., Raphael, A. P., Huang, H., and Kendall, M. A. F., 2011, "The viscoelastic, hyperelastic and scale dependent behaviour of freshly excised individual skin layers.," Biomaterials, **32**(20), pp. 4670–81.

[21]   Crichton, M. L., Chen, X., Huang, H., and Kendall, M. A. F., 2013, "Elastic modulus and viscoelastic properties of full thickness skin characterised at micro scales.," Biomaterials, **34**(8), pp. 2087–97.

[22]   Wu, J. Z., Dong, R. G., Smutz, W. P., and Schopper, A. W., 2003, "Nonlinear and viscoelastic characteristics of skin under compression: experiment and analysis.," Biomed. Mater. Eng., **13**(4), pp. 373–85.

[23]   Pubols, B. H., 1982, "Factors affecting cutaneous mechanoreceptor response. I. Constant-force versus constant-displacement stimulation.," J. Neurophysiol., **47**(3), pp. 515–29.

[24]   Craig, J. C., 1999, "Grating orientation as a measure of tactile spatial acuity," Somatosens. Mot. Res., **16**(3), pp. 197–206.

[25]   Goodwin, A. W., John, K. T., and Marceglia, A. H., 1991, "Tactile discrimination of curvature

by humans using only cutaneous information from the fingerpads.," Exp. brain Res., **86**(3), pp. 663–72.

[26] Gibson, G. O., and Craig, J. C., 2005, "Tactile spatial sensitivity and anisotropy," Percept. Psychophys., **67**(6), pp. 1061–1079.

[27] Sripati, A. P., Bensmaia, S. J., and Johnson, K. O., 2006, "A continuum mechanical model of mechanoreceptive afferent responses to indented spatial patterns.," J. Neurophysiol., **95**(6), pp. 3852–3864.

[28] Phillips, J. R., and Johnson, K. O., 1981, "Tactile spatial resolution. II. Neural representation of Bars, edges, and gratings in monkey primary afferents.," J. Neurophysiol., **46**(6), pp. 1192–203.

[29] Lesniak, D. R., Wellnitz, S. A., Gerling, G. J., and Lumpkin, E. A., 2009, "Statistical analysis and modeling of variance in the SA-I mechanoreceptor response to sustained indentation.," Conf. Proc. Annu. Int. Conf. IEEE Eng. Med. Biol. Soc. IEEE Eng. Med. Biol. Soc. Conf., **2009**, pp. 6814–7.

[30] Butler, D. L., Goldstein, S. A., and Guilak, F., 2000, "Functional tissue engineering: the role of biomechanics.," J. Biomech. Eng., **122**(6), pp. 570–5.

[31] Burns, T., Breathnach, S., Cox, N., and Griffiths, C., 2010, Rook's Textbook of Dermatology.

[32] Oomens, C. W. J., van Campen, D. H., and Grootenboer, H. J., 1987, "A mixture approach to the mechanics of skin," J. Biomech., **20**(9), pp. 877–885.

[33] Smalls, L. K., Randall Wickett, R., and Visscher, M. O., 2006, "Effect of dermal thickness, tissue composition, and body site on skin biomechanical properties.," Ski. Res. Technol., **12**(1), pp. 43–9.

[34] Tan, C. Y., Statham, B., Marks, R., and Payne, P. A., 1982, "Skin thickness measurement by pulsed ultrasound: its reproducibility, validation and variability," Br. J. Dermatol., **106**(6), pp. 657–667.

[35] Ruvolo, E. C., Stamatas, G. N., and Kollias, N., 2007, "Skin viscoelasticity displays site- and age-dependent angular anisotropy.," Skin Pharmacol. Physiol., **20**(6), pp. 313–21.

[36] Wang, Y., Marshall, K. L., Baba, Y., Lumpkin, E. A., and Gerling, G. J., 2013, "Natural variation in skin thickness argues for mechanical stimulus control by force instead of displacement," 2013 World Haptics Conference, WHC 2013, IEEE, Daejeon, Korea, pp. 645–650.

[37] Westling, G., and Johansson, R. S., 1984, "Factors influencing the force control during precision grip," Exp. Brain Res., **53**(2).

[38] Eshel, H., and Lanir, Y., 2001, "Effects of strain level and proteoglycan depletion on preconditioning and viscoelastic responses of rat dorsal skin," Ann. Biomed. Eng., **29**(2), pp. 164–172.

[39] Funk, J. R., Hall, G. W., Crandall, J. R., and Pilkey, W. D., 2000, "Linear and quasi-linear viscoelastic characterization of ankle ligaments.," J. Biomech. Eng., **122**(1), pp. 15–22.

[40] DiSilvestro, M. R., Zhu, Q., and Suh, J.-K. K., 2001, "Biphasic poroviscoelastic simulation of the unconfined compression of articular cartilage: II--Effect of variable strain rates.," J. Biomech. Eng., **123**(2), pp. 198–200.

[41] Pioletti, D. P., Rakotomanana, L. R., Benvenuti, J.-F., and Leyvraz, P.-F., 1998, "Viscoelastic constitutive law in large deformations," J. Biomech., **31**(8), pp. 753–757.

[42] Fung, Y. C., and Cowin, S. C. S. C., 1994, "Biomechanics: Mechanical properties of living

tissues," J. Appl. Mech., **61**(4), p. 1007.

[43]   Fung, Y., and Tong, P., 2001, Classical and Computational Solid Mechanics, World Scientific.

[44]   Bretag, A. H., 1969, "Synthetic interstial fluid for isolated mammalian tissue," Life Sci., **8**(5), pp. 319–329.

[45]   Lakes, R. S., 1998, Viscoelastic Solids, Taylor & Francis.

[46]   Lapczyk, I., Hurtado, J. A., and Govindarajan, S. M., 2012, "A parallel rheological framework for modeling elastomers and polymers.," 182nd Fall Technical Meeting of the Rubber Division, American Chemical Society, Cicinatti, Ohio, USA.

[47]   Holzapfel, G., 2000, "Nonlinear solid mechanics: A continuum approach for engineering."

[48]   Kent, R. W., Woods, W. A., Salzar, R. S., Damon, A. M., and Bass, C. R., 2009, "The transient relationship between pressure and volume in the pediatric pulmonary system.," J. Biomech., **42**(11), pp. 1656–63.

[49]   Laksari, K., Shafieian, M., and Darvish, K., 2012, "Constitutive model for brain tissue under finite compression," J. Biomech., **45**(4), pp. 642–646.

[50]   Gitis, N., and Sivamani, R., 2004, "Tribometrology of skin," Tribol. Trans., **47**(4), pp. 461–469.

[51]   SIMULIA, 2012, "Abaqus analysis user's manual."

[52]   Williams, A. L., Gerling, G. J., Wellnitz, S. A., Bourdon, S. M., and Lumpkin, E. A., 2010, "Skin relaxation predicts neural firing rate adaptation in SAI touch receptors.," Conf. Proc. IEEE Eng. Med. Biol. Soc., **2010**, pp. 6678–81.

[53]   Thornbury, J. M., and Mistretta, C. M., 1981, "Tactile sensitivity as a function of age.," J.

Gerontol., **36**(1), pp. 34–9.

[54]   Driskell, R. R., Jahoda, C. a B., Chuong, C.-M., Watt, F. M., and Horsley, V., 2014, "Defining dermal adipose tissue.," Exp. Dermatol., **23**(9), pp. 629–31.

[55]   Neerken, S., Lucassen, G. W., Bisschop, M. A., Lenderink, E., and Nuijs, T. A. M., 2004, "Characterization of age-related effects in human skin: A comparative study that applies confocal laser scanning microscopy and optical coherence tomography.," J. Biomed. Opt., **9**(2), pp. 274–81.

[56]   Müller-Röver, S., Handjiski, B., van der Veen, C., Eichmüller, S., Foitzik, K., McKay, I. A., Stenn, K. S., and Paus, R., 2001, "A comprehensive guide for the accurate classification of murine hair follicles in distinct hair cycle stages.," J. Invest. Dermatol., **117**(1), pp. 3–15.

[57]   Kim, E. K., Gerling, G. J., Bourdon, S. M., Wellnitz, S. A., and Lumpkin, E. A., 2012, "Force sensor in simulated skin and neural model mimic tactile sai afferent spiking response to ramp and hold stimuli," J. Neuroeng. Rehabil., **9**(1), p. 45.

[58]   Goodwin, A. W., and Wheat, H. E., 1999, "Effects of Nonuniform Fiber Sensitivity, Innervation Geometry, and Noise on Information Relayed by a Population of Slowly Adapting Type I Primary Afferents from the Fingerpad," J. Neurosci., **19**(18), pp. 8057–8070.

[59]   Goodwin, a W., Browning, a S., and Wheat, H. E., 1995, "Representation of curved surfaces in responses of mechanoreceptive afferent fibers innervating the monkey's fingerpad.," J. Neurosci., **15**(1 Pt 2), pp. 798–810.

[60]   Goodwin, A. W., Macefield, V. G., and Bisley, J. W., 1997, "Encoding of object curvature by tactile afferents from human fingers.," J. Neurophysiol., **78**(6), pp. 2881–8.

[61]   Wang, Y., Marshall, K. L., Baba, Y., Lumpkin, E. A., and Gerling, G. J., 2015, "Compressive

Viscoelasticity of Freshly Excised Mouse Skin Is Dependent on Specimen Thickness, Strain Level and Rate," PLoS One, **10**(3), p. e0120897.

[62] Plikus, M. V, and Chuong, C.-M., 2008, "Complex hair cycle domain patterns and regenerative hair waves in living rodents.," J. Invest. Dermatol., **128**(5), pp. 1071–80.

[63] Plikus, M. V, Mayer, J. A., de la Cruz, D., Baker, R. E., Maini, P. K., Maxson, R., and Chuong, C.-M., 2008, "Cyclic dermal BMP signalling regulates stem cell activation during hair regeneration.," Nature, **451**(7176), pp. 340–4.

[64] Plikus, M. V, Widelitz, R. B., Maxson, R., and Chuong, C.-M., 2009, "Analyses of regenerative wave patterns in adult hair follicle populations reveal macro-environmental regulation of stem cell activity.," Int. J. Dev. Biol., **53**(5-6), pp. 857–68.

[65] Hudson, K. M., Condon, M., Ackerley, R., McGlone, F., Olausson, H., Macefield, V. G., and Birznieks, I., 2015, "Effects of Changing Skin Mechanics on the Differential Sensitivity To Surface Compliance By Tactile Afferents in the Human Finger Pad," J. Neurophysiol., p. jn.00176.2014.

[66] Khalsa, P. S., Lamotte, R. H., and Grigg, P., 1997, "Tensile and Compressive Responses of Nociceptors in Rat Hairy Skin," J Neurophysiol, **78**(1), pp. 492–505.

[67] Iggo, A., and Muir, A. R., 1969, "The structure and function of a slowly adapting touch corpuscle in hairy skin.," J. Physiol., **200**(3), pp. 763–96.

[68] SIMULIA, 2014, Abaqus Analysis User's Guide.

[69] Lesniak, D. R., and Gerling, G. J., 2009, "Predicting SA-I mechanoreceptor spike times with a skin-neuron model," Math. Biosci., **220**(1), pp. 15–23.

[70]   Gill, P. E., and Wong, E., 2012, "Sequential Quadratic Programming Methods," Mixed Integer Nonlinear Programming, pp. 513–529.

[71]   Vega-Bermudez, F., Johnson, K. O., and Hsiao, S. S., 1991, "Human tactile pattern recognition: active versus passive touch, velocity effects, and patterns of confusion," J Neurophysiol, **65**(3), pp. 531–546.

[72]   Shou, W., Bergstrom, C. T., Chakraborty, A. K., and Skinner, F. K., 2015, "Theory, models and biology," Elife, **4**, pp. 1–4.

[73]   Eastwood, A. L., Sanzeni, A., Petzold, B. C., Park, S.-J., Vergassola, M., Pruitt, B. L., and Goodman, M. B., 2015, "Tissue mechanics govern the rapidly adapting and symmetrical response to touch," Proc. Natl. Acad. Sci., **112**(50), pp. E6955–E6963.

[74]   Werner, G., and Mountcastle, V. B., 1965, "Neural activity in mechanoreceptive cutaneous afferents: stimulus-response relations, weber functions, and information transmission.," J. Neurophysiol., **28**(2), pp. 359–97.

[75]   Ge, W., and Khalsa, P. S., 2002, "Encoding of compressive stress during indentation by slowly adapting type I mechanoreceptors in rat hairy skin.," J. Neurophysiol., **87**(4), pp. 1686–93.

[76]   Kaim, L., and Drewing, K., 2011, "Exploratory Strategies in Haptic Softness Discrimination Are Tuned to Achieve High Levels of Task Performance," IEEE Trans. Haptics, **4**(4), pp. 242–252.

[77]   Kumar, S., Liu, G., Schloerb, D., and Srinivasan, M. a., 2015, "Viscoelastic Characterization of the Primate Finger Pad in vivo by Micro-step Indentation and 3D Finite Element Models for Tactile Sensation Studies," J. Biomech. Eng., **137**(June), pp. 1–10.

[78]   Wu, J. Z., Dong, R. G., Rakheja, S., Schopper, A. W., and Smutz, W. P., 2004, "A structural fingertip model for simulating of the biomechanics of tactile sensation.," Med. Eng. Phys., **26**(2), pp. 165–75.

[79]   Gerling, G. J., and Thomas, G. W., 2008, "Fingerprint lines may not directly affect SA-I mechanoreceptor response.," Somatosens. Mot. Res., **25**(1), pp. 61–76.